# Influence of Pressure on Supersonic Retropropulsion Flow Field at Mach 2

Yibing Maxine Tan

A thesis
submitted in partial fulfillment of the
requirements for the degree of

Master of Science

University of Washington
2018

Committee:
Owen Williams
Carl Knowlen

Program Authorized to Offer Degree:
College of Engineering,
William E. Boeing Department of Aeronautics and Astronautics

University of Washington

## Abstract

Experimental Investigation of Supersonic Retropropulsion

Yibing Maxine Tan

Chair of Supervisory Committee:
Owen Williams
Department of Aeronautics and Astronautics

The effectiveness of Supersonic Retropropulsion is difficult to predict due to the many parameters that can influence the flow field. This thesis uses a combination of control volume and dimensional analyses to propose a minimal set of parameters that are likely to be the primary influencers of this flow interaction. As the most prominent parameter, the influence of stagnation pressure ratio between the jet and freestream flows was experimentally examined using a Ludwieg Tube and schlieren photography. This flow visualization is analyzed quantitatively to identify flow unsteadiness based on measurements of bow shock topography, motion, standoff distance and curvature. Principal Component Analysis (PCA) was also used to identify regions of flow unsteadiness and major flow structures.

**Acknowledgements**

I would like to thank my advisor, Owen Williams, for his guidance and encouragement throughout this thesis. His mentorship and support has allowed me to explore and conduct my research, despite bumps on the road. He has taught me so much, both academically and about the world, and I am very thankful.

This experimental investigation would not have been possible without the generosity of Carl Knowlen, who graciously allowed us to share his lab space and equipment. Also, experiments would have not been as successful, or at least taken much longer, without the assistance of Charlie Yang and Brenton Ho, who helped me through the countless hours. Lastly, the high-speed camera used comes courtesy of the Student Technology Fund at the University of Washington.

I would also like to thank my friends and colleagues for the conversations and experiences we've shared and their endless love for me despite how difficult I can be. A big thank you to my colleagues Antonio Deleo, Abhiram Aithal, Sean Phenisee, Hoang Nguyen Minh, Pablo Trefftz, Gustavo Fujiwara and Luke Richards for creating a conducive environment with such a love for learning, and exchanging knowledge and ideas about academics, the world and life. Also, thank you to Trever Byrd, Charlie Pecora, Navi Sandhu, and Jon Frydman who journeyed with me through our Masters and have been such amazing friends through some very difficult times. I am also thankful for Roy Sebastian Djunaidi, Kay Shigemori and Molly Zhang, who have always believed in me and have the amazing ability to make me feel like I belong.

I would also like to thank Robert Breidenthal, a teacher and mentor with wisdom beyond his years. He has taught me to follow my heart and trust in myself, even though there are times when the universe seems against you.

Finally, I would like to thank my parents and family for their love, blessing and kindness through my education and growth. They have always encouraged me to follow my passion and supported me through my education and growth. They have taught me about life and how to live, and love and how to give. I would not be where I am without all they have sacrificed. Words cannot describe how grateful I am and how much this means to me.

# Table of Contents

# List of Figures

# List of Tables

# 1. Introduction

Today, the new space race approaches its peak as corporations compete to send the latest satellites to space, explore new frontiers and colonize neighboring planets such as Mars. While the industry is relatively confident with their capability to launch rockets into space, the new challenge is to successfully land these rockets, either back for reuse or to other planets for delivery of ever larger payloads.

Classically, the technology associated with the Entry, Descent and Landing (EDL) of rockets is that of giant parachutes to decelerate a spacecraft. However, the parachute deceleration technique is not a viable option for vehicles with large ballistic coefficient (Korzun & Braun, 2010),

$$\beta = \frac{m}{C_D A}$$

where $m$ is the mass of the rocket, $C_D$ is the drag coefficient of the rocket configuration and $A$ is the cross-sectional area of the rocket descent configuration. For vehicles with large ballistic coefficients travelling at supersonic speeds, it is hard to determine the deploying dynamics of the parachutes and parachutes simply do not provide enough deceleration. The inconsistencies that arise from the difficulty in predicting loads results in performance uncertainty and possible failure. The system is very complicated and have experimentally failed to be successful in decelerating the heavier and bulkier payloads. For instance, failed NASA experiments with the Low-Density Supersonic Decelerator (LDSD) vehicle demonstrate that the technological limit for size and weight with the parachute deceleration technology has been reached. Because the parachute deceleration technique cannot be scaled up for the increased payloads, a more robust deceleration technique to slow down from a hypersonic re-entry into a thin atmosphere to a subsonic landing is required.

Supersonic Retropropulsion (SRP) presents a promising solution to the problem. SRP is achieved by directing thrust from an engine into the oncoming flow of the atmosphere to decelerate a supersonic re-entry vehicle. The technology behind SRP is relatively simple, scalable for larger rockets, reusable and most likely to provide mission assurance for large spacecraft EDL. Moreover, the components for the construction and implementation of the SRP technology, such as heat-resistant leading-edge nozzles and propulsion engines are readily available as well. Preliminary studies suggest that SRP can also reduce heating on the rocket for increased reusability.

However, additional research is essential to understand SRP flow field unsteadiness and topology for improved control and effective execution. Also, a better prediction of retropropulsive forces is necessary to minimize damage.

The studies investigating SRP flow field behavior have identified regimes of severe flow unsteadiness that are affected by parameters such as thrust coefficient, pressure ratio, mass flow rate, Mach number, etc. However, while qualitative flow field interactions have been observed, it is uncertain to what extent SRP flow interactions

a) characterize the regimes of steadiness and unsteadiness in SRP flow
b) are quantitatively affected by identified and investigated parameters
c) are affected by other unidentified and uninvestigated parameters
d) are influenced by independent variation or coupled effect of the parameters

In other words, SRP flow is not understood well and that makes prediction poor. This limitation is holding back the development of SRP as the primary rocket deceleration technique. This thesis aims to propose a minimal subset of parameters that dominate flow field dynamics so as to

predict and replicate SRP flow behavior for different conditions. Hence, this thesis will perform a parametric study on the problem with a control volume analysis and dimensional analysis that identifies what we propose to be the important parameters for the SRP flow field. This study selects the stagnation pressure ratio between the retronozzle jet and the freestream flow as the parameter to experimentally investigate for regimes of flow unsteadiness.

# 2. Background

For SRP to be effective, the deceleration achieved by SRP must increase the overall retarding force experienced by the vehicle. This is quantitatively measured with the concept Aerodynamic Drag Preservation which analyzes how to maintain the deceleration force from a vehicle's aerodynamic drag while increasing the overall retarding force with SRP deceleration. This concept was introduced in the early stages of SRP research (Charczenko & Hennessey, 1961) and reiterated for recent SRP performance analysis is explained in detail below.

## 2.1. Aerodynamic Drag Preservation

In order to compare the decelerating force contributions from aerodynamic drag and the jet thrust for different flow conditions, non-dimensional coefficients are introduced for each force.

Firstly, there is the aerodynamic drag coefficient ($C_D$) which is an inherent property of the vehicle geometry that decelerates the vehicle, and it is given below:

$$C_D = \frac{F_D}{\frac{1}{2}\rho_\infty {U_\infty}^2 A_{forebody}}$$

where $F_D$ is the drag force, $\frac{1}{2}\rho_\infty {U_\infty}^2$ is the dynamic pressure of the freestream and $A_{forebody}$ is the forebody area. While the aerodynamic coefficient can be simulated with vehicle forebody geometry and freestream properties, it is usually found experimentally by integrating the surface pressure distribution on the forebody.

Secondly, there is the jet thrust coefficient ($C_\Psi$), the primary parameter for characterizing jet flow conditions, and it is given by:

$$C_\Psi = \frac{\Psi}{\frac{1}{2}\rho_\infty {U_\infty}^2 A_{forebody}}$$

where $\Psi$ is the jet thrust, $\frac{1}{2}\rho_\infty {U_\infty}^2$ is the dynamic pressure of the freestream and $A_{forebody}$ is the forebody area.

Next, it is useful to introduce the total axial force coefficient of the forebody ($C_F$), which characterizes the overall non- dimensional deceleration force experienced by the vehicle. The total axial force coefficient is the sum of the deceleration force from aerodynamic drag ($C_D$) and the deceleration force from the jet thrust ($C_\Psi$), given below, and offers a quantitative insight into the contributing deceleration forces.

$$C_F = C_D + C_\Psi$$

To use SRP efficiently and ideally, increasing the jet thrust ($C_\Psi$) should cause a direct increase of the overall deceleration and total axial force ($C_F$) while maintaining and preserving the contribution of aerodynamic drag ($C_D$) deceleration. The loss of the aerodynamic drag contribution occurs when the disruption of the flow in front of the forebody from the jet plume creates a pocket such that the shape of the forebody no longer interacts with the freestream flow as strongly. The total axial force may increase, but the increasing proportion of that is just due to thrust, which reduces the overall efficiency. (Korzun, Braun, & Cruz, 2009).

It is generally observed, in Figure 1 (Korzun, Braun, & Cruz, 2009), that increasing the thrust coefficient decreases the aerodynamic drag coefficient to a constant minimum of approximately 10% of the aerodynamic drag value with no jet. As thrust coefficient increases further, it contributes to the total axial force coefficient in proportional increments. These trends are illustrated below in a figure adapted from results (McGhee, 1971) of experimentation with a single central nozzle.

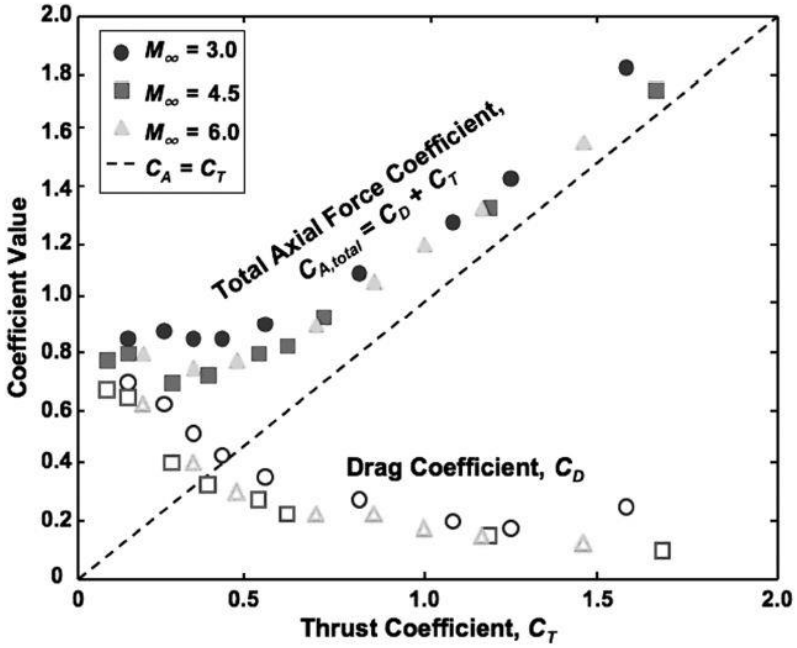


**Figure 1: The Variation of Aerodynamic Drag Coefficient and Total Axial Force Coefficient with Increasing Thrust Coefficient (Korzun, Braun, & Cruz, 2009)**

The aforementioned trends can be attributed to the shape of the contact surface (the bow shock topography) that is a result of the nozzle configuration and strength of the retronozzle jet flow (Korzun & Braun, 2010). When the bow shock surface is even, there are high surface pressures on the forebody that contributes to aerodynamic drag. Conversely, in cases where the bow shock is penetrated and with an uneven surface, there is a reduced surface pressure on the forebody due to the freestream flow being unable to reach the forebody (Korzun, Cordell, & Braun, 2010). The degree of surface pressure reduction is proportional to the Mach number (McGhee, 1971).

The total axial force coefficient ($C_{\mathrm{F}}$) is an important concept in the practical implementation and performance evaluation of SRP, and it will be used for the control volume analysis and dimensional analysis in this thesis.

## 2.2. Effect of forebody geometry

For most vehicles, there are two geometrical options that are known to significantly influence the flow field– the retronozzle jet configuration and the area ratio between the retronozzle jet exit and the forebody.

First, the two most examined retronozzle jet configurations, as seen in Figure 2, are the central nozzle configuration and the peripheral tri-nozzle configuration as they are most understood. Note that the third configuration often studied is the quad-nozzle configuration which is a combination of the two aforementioned nozzle configurations

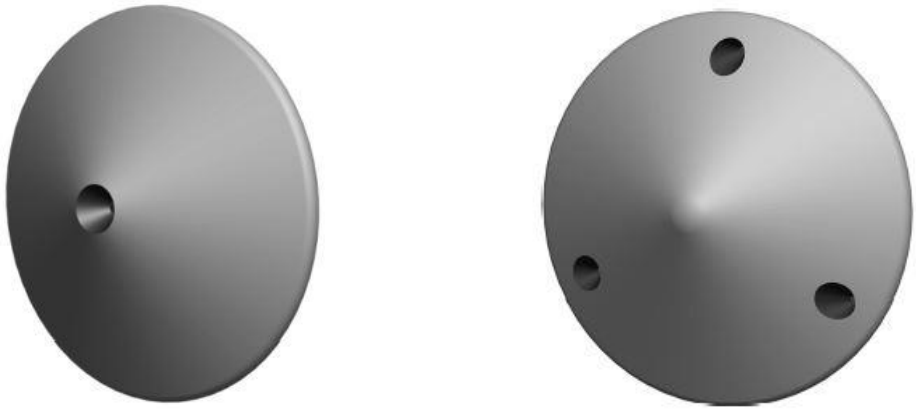

**Figure 2: Nozzle Configuration, (left) Central Nozzle and (right) Peripheral Tri-Nozzle (Korzun, Braun, & Cruz, 2009)**

For the central and peripheral tri-nozzle two configurations mentioned above, their respective characteristic flow field behavior for a significantly under-expanded jet is illustrated below in Figure 3. For both configurations, there is a detached bow shock, a recirculation region and a jet terminal shock at the downstream end of the retronozzle jet flow. For an under-expanded jet, the retronozzle jet flow pressure is much higher compared with the surrounding pressure and this results in the jet terminal shock when the jet flow attempts to pressure match. The area between

both flows is less supersonic than the freestream or jet flow, and the interaction between the opposing flows causes recirculation and mixing.

The under-expansion condition of the central nozzle configuration jet in Figure 3a is most commonly studied as it is the most likely condition in practical situations given the thin atmosphere for vehicle entry and most nozzles are sized for sea-level expansion conditions. However, note that variable engine nozzles or engine nozzles designed for upper atmosphere SRP scenarios specific for reentry will produce different jet expansion conditions.

Although the SRP flow field for both configurations have similar features, such as the detached bow shock, the retronozzle jet terminal shock and the recirculation regions, both configurations result in a vastly different flow field. This is due to the different physical interaction between the retronozzle jet and freestream flow that demonstrate a clear geometric dependence on SRP flow field behavior. For instance, studies have indicated that the peripheral tri-nozzle configuration produces results in more flow field unsteadiness than the central nozzle configuration (Berry, Rhode, Edquist, & Player, 2011).

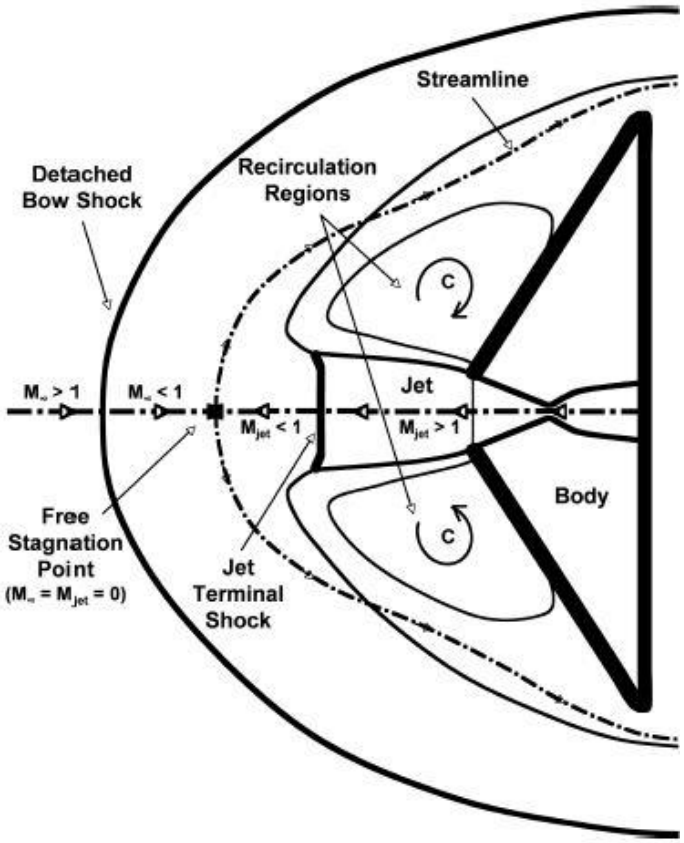


**(a)**

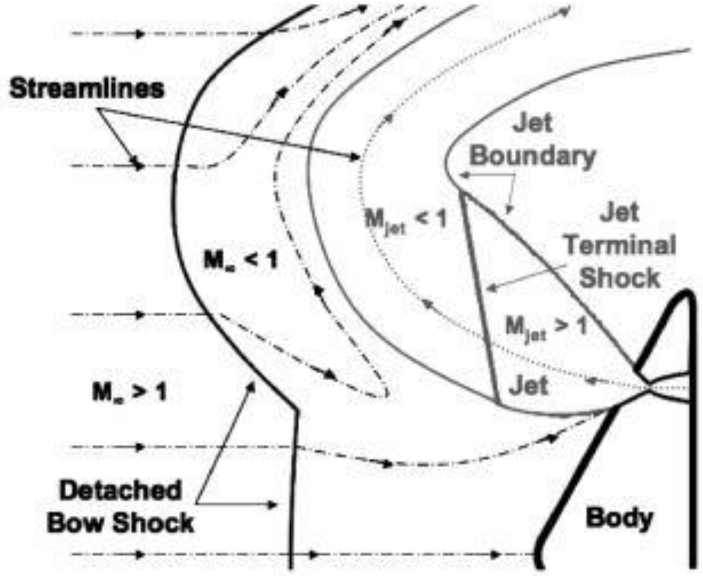


**(b)**

**Figure 3: Characteristic Flow Field Features of Under-Expanded Jet for (a) Central Nozzle and (b) Peripheral Tri-Nozzle (Korzun, Braun, & Cruz, 2009)**

Secondly, it has been found that the area ratio of the retronozzle jet exit and forebody area is inversely proportional to the extent of bow shock penetration (Venkatachari, Cheng, Chang, Zichettello, & Bilyeu, 2013). In other words, the smaller the relative area of the retronozzle jet exit to the forebody, the larger the likelihood that the retronozzle jet flow will penetrate the bow shock causing unsteadiness. This is likely because the smaller retronozzle jet exit allows more momentum to be carried downstream of the jet flow because of the relative increased forebody area deflecting the freestream flow. As such, the extent of bow shock penetration is dependent on the expansion condition of the retronozzle jet flow.

This thesis will only investigate the limiting case of the central nozzle configuration with no forebody.

## 2.3. Retronozzle Jet Expansion

The retronozzle jet expansion pattern is dependent on the ratio of static pressure at the jet exit and the ambient pressure ($P_j/P_a$). For a jet flow, the value of $P_a$ is the surrounding ambient pressure while for SRP flow, the value of $P_a$ is the upstream pressure of the freestream before the detached bow shock. The three jet expansion patterns, relative to increasing stagnation pressure ratio, are roughly classified as the over-expanded jet, the moderately under-expanded jet and the highly under-expanded jet as depicted in Figure 4. Note that for a fixed supersonic nozzle, the over-expanded jet is subsonic after the initial shocks in its flow expansion pattern while the two variations of the under-expanded jet are supersonic.

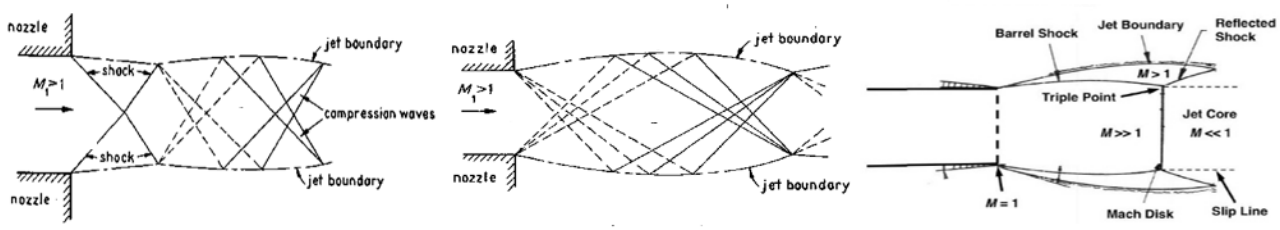


**Figure 4: Retronozzle Jet Expansion Pattern - (left) Over-Expanded, (middle) Moderately Under-Expanded, (right) Highly Under-Expanded**

The retronozzle jet expansion pattern affects the momentum propagation of the jet and subsequent downstream contact surface of the jet with the flow. The two flows must come together and match pressures in various regions of the flow through expansion or compression waves, or produce shocks.

For an over-expanded jet, the $P_j/P_a$ ratio is lower than unity. At the jet exit, there is an oblique shock as the atmosphere pressure matches with the lower jet pressure. Then, there is a series of expansion and compression waves that results in an ellipsoid shape of the jet exhaust with a slightly oblique contact surface. Because of the shallow pressure gradient, the jet only requires a relatively short distance to pressure match the jet flow with atmosphere and there is less momentum propagated downstream as the jet exhaust is subsonic.

For a moderately under-expanded jet, the $P_j/P_a$ ratio is around unity. In this case, the pressure gradient is not steep enough for shocks, and the jet exhaust can only pressure match the atmosphere with a series of expansion waves. The expansion waves only change the pressure slightly, which mean an increased distance is required for the pressure matching. This causes a flatter ellipsoid shape of the jet with a sharp oblique contact surface. Also, this means that there is more momentum propagated downstream as the jet exhaust is supersonic.

For a highly under-expanded jet, the $P_j/P_a$ ratio is above unity. The pressure gradient is very high which requires a strong normal shock to pressure match the supersonic jet exhaust with the atmosphere. This is achieved with the Mach disk terminal shock that results in a flat contact surface and a subsequent subsonic flow downstream. Theoretically, the distance required to pressure match is less than for the moderately under-expanded jet. However, the initial high momentum of the jet exhaust is unlikely to be solely dissipated by the Mach disk terminal shock, even though it does drastically reduce the momentum. This is seen with the more compact ellipsoid shape of the jet exhaust that extends past the Mach disk terminal shock, which suggests there is an increased radial momentum propagation.

As mentioned earlier, the highly under-expanded jet is the most common jet expansion pattern for landing first-stage boosters on Earth and the flow field structure will be elaborated. The supersonic freestream and jet flow meet at a free stagnation point. The supersonic freestream flow is decelerated by the detached bow shock to a subsonic flow and then to zero velocity while the jet flow is decelerated by the terminal jet shock, and viscous dissipation and mixing. The flow between the two supersonic regions (as the freestream and jet flow decelerates) is subsonic that consists of a recirculation region along the surface of the forebody and a shear layer. The shear layer is a result of the steep velocity and pressure gradients between the interaction of the freestream and jet flows, hence, it can be thought of being representative of the outer jet boundary (Korzun, Cordell, & Braun, 2010). The shear layer is also very turbulent as it transfers and superimposes the disturbances from the opposing flows.

Consideration of the expansion condition of the supersonic retronozzle is useful because it provides an intuitive physical visualization of the jet exhaust in SRP flow field interaction. While $P_j/P_a$ ratio is most commonly used to characterize the retronozzle jet expansion pattern, it can

also be equivalently described with other parameters, such as stagnation pressure ratio, jet mass flow rate, jet thrust coefficient or even surface pressure measurements.

## 2.4. Regimes of SRP Flow Field Steadiness

SRP flow steadiness is important for successful implementation as it has a significant impact on load modelling and prediction for stability and control. In general, regimes classified are described by bow shock steadiness – its standoff distance, its oscillatory motion, the extent of its penetration and its topography. Flow visualization methods, experimental and computational, such as shadowgraphy, schlieren photography and CFD with quantitative measurements are some common techniques used to study SRP flow steadiness.

Most experiments vary a property of the jet and then try to characterize the steadiness of the SRP flow interaction by observing bow shock motion. As mentioned, the jet properties varied, which include the stagnation pressure ratio between the jet and the freestream (Jarvinen & Adams, 1970), jet driving stagnation pressure (Daso, Pritchett, Wang, Ota, & Blankson, 2007), static pressure ratio between the jet and the freestream (McGhee, 1971), jet mass flow rate (Barber, 1965), jet thrust coefficient (Finley, 1966), are just different ways of describing the jet expansion pattern and are often used interchangeably. For instance, Finley (1966) investigated counterflowing jets for a Mach 2.5 freestream with varying jet sizes of a sonic and Mach 2.6 jet. His analysis shows that the jet expansion pattern, explained using the jet Mach number and "flow-force coefficient" are critical for determination of flow steadiness.

When considering bow shock steadiness, a common concept is to talk about the bow shock topography and its penetration by the retronozzle jet exhaust. These different types of flow field interactions are often characterized into regimes. For example, Warren (1959) experimentally investigated the effects of SRP cooling capabilities by ejecting coolant gases, such as Nitrogen

and Hydrogen, against a freestream Mach 5.8 flow. He noted two flow regimes – the first regime was at lower jet flow rates with lower jet momentum which did not disturb the bow shock structure while the second regime was at jet flow rates with sufficiently high enough momentum to cause the bow shock structure to "bulge" out. This observation of bow shock topography was also made by Romeo & Sterrett (1963) who investigated the effect of a forward-facing jet on the bow shock of blunt body for a Mach 6 freestream. They identified two modes of SRP flow interactions – the first mode where the bow shock retained its structure but grew in size, while the second mode for increasing Mach number and higher stagnation pressure ratio where the bow shock standoff distance increased and the flow was more unstable. A good label for the observed bow shock topography is coined by Jarvinen & Adams (1970) who described two regimes of bow shock jet penetration. There is the long-penetration mode of the bow shock at low jet thrust coefficients and the short-penetration mode at high jet thrust coefficient when the jet exhaust is terminated by a Mach disk terminal shock. Likewise, McGhee (1971) identified four different regimes determined by the jet thrust coefficient and static pressure ratio. These are observed in Figure 5 below. In Regime 1, the jet is over-expanded; in Regime 2, the jet is fully expanded; in Regime 3, the jet is moderately under- expanded; in Regime 4, the jet is highly under-expanded. It was noted that Regimes 1 and 2 were unsteady while Regimes 3 and 4 were steady. For the steady regimes, it was found that the locations of the jet exhaust Mach disk terminal shock, the flow interface and the bow shock were functions of nozzle thrust coefficient. Recently, Daso, Pritchett, Wang, Ota, & Blankson (2007) also perfromed CFD with varying stagnation pressure ratios that produced supporting results illustrating the various possible extents of bow shock jet penetration as seen in Figure 6.

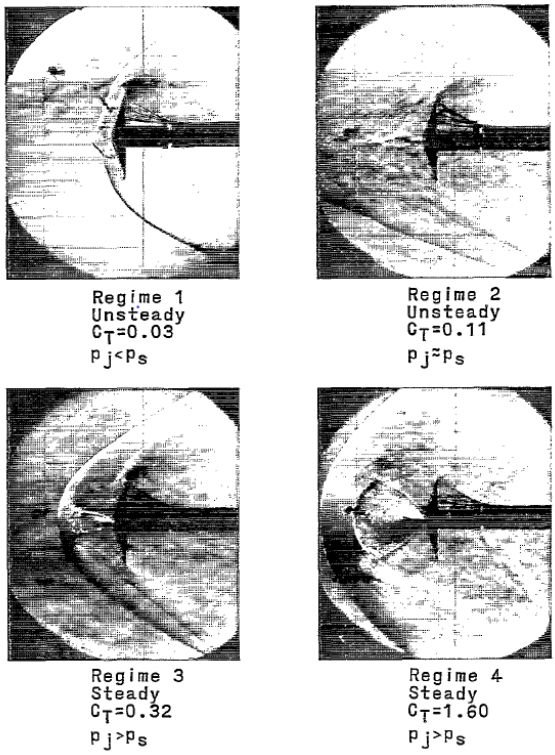


**Figure 5: SRP Flow Interaction Regimes (McGhee, 1971)**

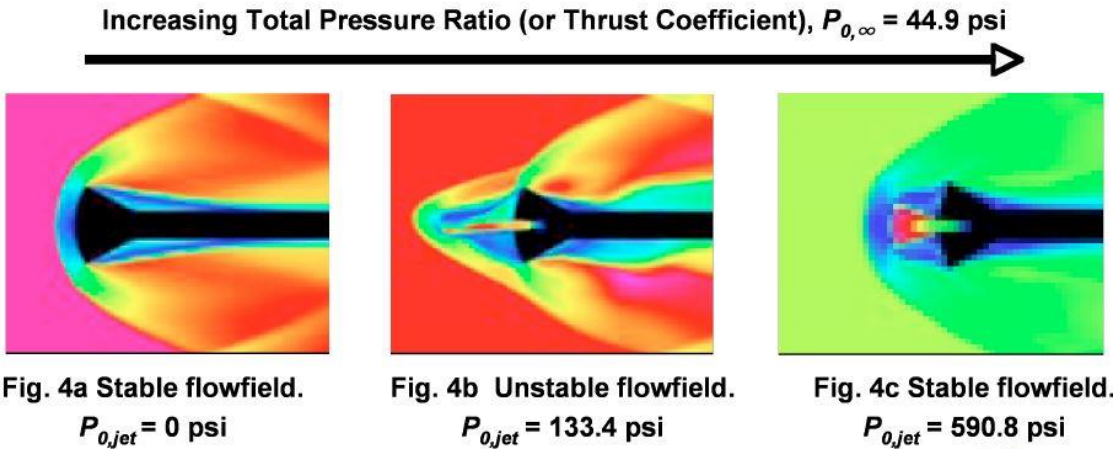


**Figure 6: SRP Flow Interaction Regimes (Daso, Pritchett, Wang, Ota, & Blankson, 2007)**

On another note, Shang, Hayes, Wurtzler, & Strang (2001) provide a physical explanation of the bow shock bifurcation with a resonance theory between the free-shear-layer instabilty and the retronozzle jet exhaust contact surface. They used this feedback loop to explain the unsteadiness of the regimes – an unsteady "subcritical" state with oscillatory motion and a steady

“supercrictical” state after the bow shock bifurcation point, which are controlled by the stagnation pressure ratio between the jet and the freestream flow. Likewise Hiyashi, Aso, & Tani (2005) conducted a numerical analysis that showed how the observed feedback between the recirculation region and the jet boundary layer casues oscillation and unsteadiness.

## 2.5. Bow Shock Unsteadiness

From previous results, there is a direct relationship between the jet expansion pattern and the penetration of the bow shock. There is also strong correlation between the bow shock penetration and the unsteadiness of the flow. For over-expanded and highly under-expanded jets, they observe the “short penetration mode” (SPM) where the jet exhaust does not affect the even bow shock topography. Alternatively, for perfectly expanded and moderately under-expanded jets, they observe the “long penetration mode” (LPM) where the jet exhaust penetrates through the bow shock which results in an uneven bow shock topography. For SPM, the bow shock is clearly defined with a steady standoff distance from the forebody. For LPM, the bow shock appears weaker with penetration that causes uneven bow shock standoff distance and oscillatory motion.

This thesis suggests that this phenomenon can be explained by considering the momentum the jet exhaust possesses when interacting with the freestream flow. For SPM, the jet exhaust has a blunt contact surface and relatively lower momentum due to energy dissipation from the jet expansion pattern. There are shocks present in the jet exhaust which allows drastic changes in pressure for more efficient pressure matching. In contrast, for LPM, the jet exhaust has a sharp oblique contact surface with the freestream and a relatively much higher momentum due to the series of expansion and compression waves which only result in lower pressure changes for less efficient pressure matching that increases the space needed to match pressures. In most cases, the SPM is likely to be steady while the LPM is likely unsteady.

Alternatively, quantitative measurements of bow shock steadiness such as bow shock standoff distance and curvature vary across SPM and LPM. For instance, the bow shock standoff distance, measured from the tip of the bow shock, is longest for LPM, it is shorter for SPM of the highly under-expanded jet and shortest for SPM of the over-expanded jet. This result was found by Barber (1965) and can be seen in Figure 7.

Note that bow shock standoff distance can be difficult to determine accurately due to the nature of flow visualization techniques that integrate across the flow field. This means it is likely that the forward penetrated tip of the bow shock is not always clearly visible.

For unsteady flows, the bow shock region tends to oscillate and bow shock motion frequency can be used to determine steadiness. This definition of bow shock steadiness is what this thesis will investigate.

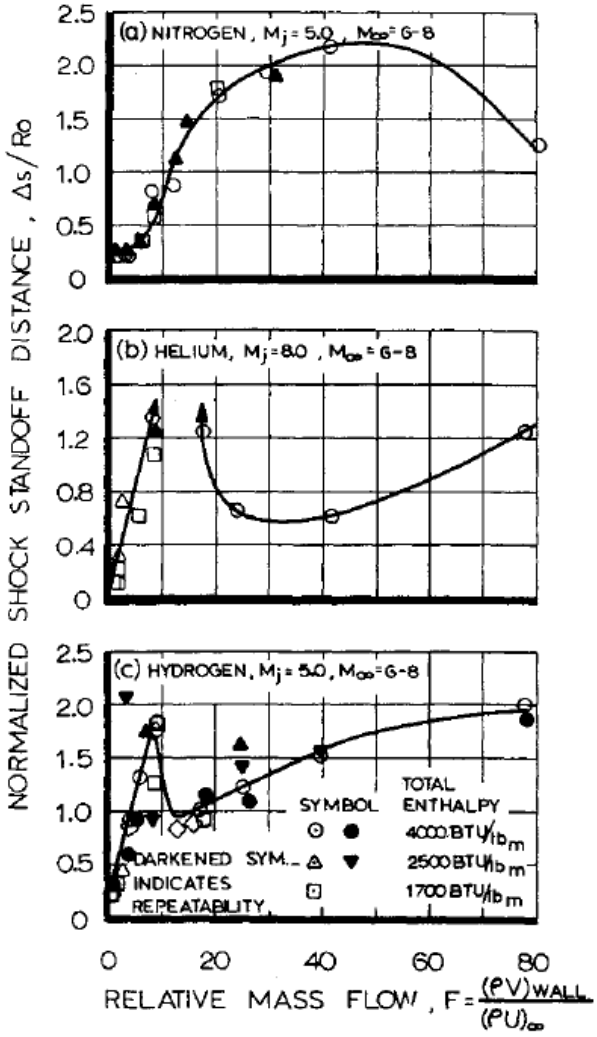


**Figure 7: Bow Shock Standoff Distance with Jet Mass Flow Rate (Barber, 1965)**

## 2.6. The problem

There are several unanswered questions about SRP technology that include, but are not limited to:

a) How to achieve Aerodynamic Drag Preservation and ensuring that the contribution from jet exhaust improves deceleration efficiently

b) Find the optimal geometrical configuration for maximal jet exhaust deceleration effects

c) Investigate the full range of independent parameters and their influence on SRP flow steadiness. These parameters need to be identified.
d) Characterize regimes of steadiness qualitatively and quantitatively.

This thesis will mainly focus on (c). While it is understood well that the jet expansion patterns, and equivalent parameter characterizations, influence SRP flow field, this thesis argues for a simplified set of flow parameters and identifies relationships between previously used parameters and those suggested here. These independent parameters should be investigated to analyze its influence on SRP flow field behavior and characterize regimes of steadiness due to the promise that it will lead to better physical insight into SRP flow and allow the development of a more robust modelling and prediction of the flow field. This thesis will choose the most important parameter and conduct a series of experiments which will examine the SRP flow field, its topology and unsteadiness as a function of that parameter.

# 3. Theory

In this section, a control volume analysis and dimensional analysis will be performed on the SRP flow field problem so as to identify the pertinent parameters.

## 3.1. Control Volume Analysis:

The thrust $\Psi$ used to calculate thrust coefficient $C_\Psi$ can be approximated using a control volume analysis of the jet. It is hypothesized that this coefficient is dependent on the jet properties and the relationship between jet exit and nozzle throat conditions. Note that this analysis assumes the limiting case with infinitely small forebody area that is neglected.

The entrance of the jet is connected to a pressurized tank while the exit of the jet is directed towards an oncoming supersonic flow. The control volume selected contains the isentropic jet nozzle from its throat (corresponding to the numbered subscript '1') to its exit (corresponding to the numbered subscript '2'), as pictured below in the diagram. At the inlet and outlet of the control volume, the properties at each station include the specific gas constant ($R_j$) and heat capacity ratio ($\gamma_j$) of the jet and the pressure ($P$), density ($\rho$), temperature ($T$), velocity ($U$) and area ($A$).

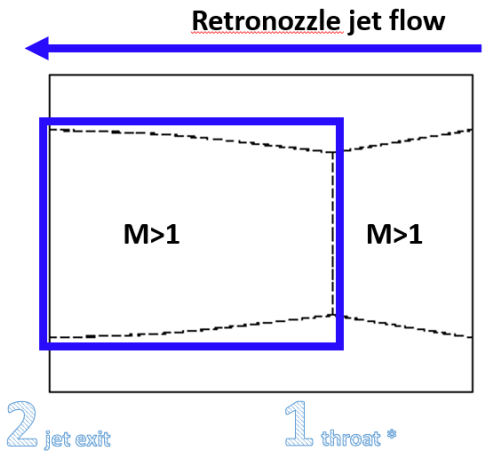


**Figure 8: Control Volume of Retronozzle Jet**

Note that because the control volume starts at the choked throat, the Mach number there is known.

$$M_1 = 1 = \frac{U_1}{\sqrt{\gamma_1 R_1 T_1}}$$

The thrust $\Psi$ is calculated through a momentum balance:

$$\Psi = \sum F = \sum \dot{m}\, U + P\, A = [\, \dot{m}\, U + P\, A\, ]_2 - [\, \dot{m}\, U + P\, A\, ]_1$$

where $\dot{m}$ is the mass flow rate, which is defined by the following equation

$$\dot{m} = \rho\, U\, A$$

Therefore, the force balance can be expanded to the following form:

$$\Psi = \rho_2\, U_2^2\, A_2 - \rho_1\, U_1^2\, A_1 + P_2 A_2 - P_1 A_1$$

Next, the thrust equation is normalized with respect to the freestream dynamic pressure ($\frac{1}{2}\rho_\infty U_\infty^2$) and the forebody area ($A_{forebody}$) to create a non-dimensional thrust coefficient as seen below. This normalization parameter ($\frac{1}{2}\rho_\infty U_\infty^2\, A_{forebody}$) was chosen for consistency with non-dimensionalization of the aerodynamic drag coefficient ($C_D$) and the total axial force coefficient ($C_F$).

$$C_\Psi = \frac{\rho_2\, U_2^2\, A_2}{\frac{1}{2}\rho_\infty U_\infty^2\, A_{forebody}} - \frac{\rho_1\, U_1^2\, A_1}{\frac{1}{2}\rho_\infty U_\infty^2\, A_{forebody}} + \frac{P_2}{\frac{1}{2}\rho_\infty U_\infty^2}\frac{A_2}{A_{forebody}} - \frac{P_1}{\frac{1}{2}\rho_\infty U_\infty^2}\frac{A_1}{A_{forebody}}$$

Because the throat is choked, the velocity at the throat can be expressed as:

$$U_1 = \sqrt{\gamma_1\, R_1\, T_1}$$

Consequently, the thrust coefficient ($C_\Psi$) equation can be expressed as:

$$C_\Psi = \left(\frac{A_2}{A_{forebody}}\right)\left(\frac{\rho_2\, U_2^2}{\frac{1}{2}\rho_\infty U_\infty^2} + \frac{P_2}{\frac{1}{2}\rho_\infty U_\infty^2}\right) - \left(\frac{A_1}{A_{forebody}}\right)\left(\frac{\rho_1\, \gamma_1\, R_1\, T_1}{\frac{1}{2}\rho_\infty U_\infty^2} + \frac{P_1}{\frac{1}{2}\rho_\infty U_\infty^2}\right)$$

Then, the ideal gas law is used to collect terms:

$$C_\Psi = \left(\frac{A_2}{A_{forebody}}\right)\left(\frac{\rho_2\, U_2^2}{\frac{1}{2}\rho_\infty U_\infty^2} + \frac{P_2}{\frac{1}{2}\rho_\infty U_\infty^2}\right) - \left(\frac{A_1}{A_{forebody}}\right)\left(\frac{P_1}{\frac{1}{2}\rho_\infty U_\infty^2}\right)(\gamma_1 + 1)$$

The above equation can then be rearranged to obtain the following equation:

$$C_\Psi = \left(\frac{A_2}{A_{forebody}}\right)\left[\frac{\rho_2\, U_2^2}{\frac{1}{2}\rho_\infty U_\infty^2} + \left(\frac{P_2}{\frac{1}{2}\rho_\infty U_\infty^2}\right)\left(1 - \frac{A_1}{A_2}\frac{P_1}{P_2}\,(\gamma_1 + 1)\right)\right]$$

Through observation, there are five non-dimensional parameters. These are the area ratio between the jet exit and the forebody, the momentum flux ratio between the jet exit and the freestream, the jet exit pressure coefficient, and the jet throat to exit area ratio and the jet pressure ratio between the jet throat and the jet exit:

$$A_{ratio} = \frac{A_2}{A_{forebody}}\,, \qquad J_{flux} = \frac{\rho_2\, U_2^2}{\rho_\infty U_\infty^2}\,, \qquad C_{p_j} = \frac{P_2}{\frac{1}{2}\rho_\infty U_\infty^2}\,,$$

$$A_{j_{ratio}} = \frac{A_1}{A_2}, \qquad P_{j_{ratio}} = \frac{P_1}{P_2}$$

Hence, the thrust coefficient equation can be expressed in terms of the aforementioned variables. Note that in this expression, the subscript ‘2’ for the jet exit is replaced with the subscript ‘j’:

$$C_\Psi = (A_{ratio})\left[2\, J_{flux} + \left(C_{p_j}\right)\left(1 - A_{j_{ratio}} P_{j_{ratio}}\,(\gamma_j + 1)\right)\right]$$

Consequently, the thrust coefficient is therefore dependent on the following parameters:

$$C_{\Psi} = f(A_{ratio}, A_{j_{ratio}}, J_{flux}, P_{j_{ratio}}, C_{p_j}, M_j, \gamma_j)$$

The thrust coefficient of the jet is indeed dependent on the jet parameters (jet exit Mach number $M_j$, heat capacity ratio $\gamma_j$, jet pressure coefficient $C_{p_j}$, jet area ratio $A_{j_{ratio}}$) and the relationship between jet and freestream conditions (the area $A_{ratio}$ and momentum flux $J_{flux}$). It is important to note that because all the parameters that the thrust coefficient is depending on is known and can be fixed, the thrust coefficient is essentially chosen for a given experimental test. Also, it will be shown that the parameters have their own additional dependencies, which become more relevant when analyzing the complete SRP flow field.

## 3.2. Dimensional Analysis:

Further insight into the full SRP problem can be gained through dimensional analysis. While the final list of independent parameters obtained using this method must be tested through experiment, such an analysis is useful to limit the number of such tests.

For SRP flow field behavior, the total axial force, $F$, is influenced by the following dimensional variables related to the flow properties of the freestream (subscript ∞) and jet (subscript *j*), as well as forebody and nozzle geometry:

- Static Pressure $P$
- Density $\rho$
- Temperature $T$
- Velocity $U$
- Heat Capacity Ratio $\gamma$
- Viscosity $\mu$
- Area, $A$ (forebody and nozzle)
- Nozzle Divergence Angle $\theta$
- Nozzle Angle of Attack $\alpha$

Note that the specific gas constant $R$ is not considered an independent variable as it can be expressed with the ideal gas law in terms of other variables with the following equation:

$$R = \frac{P}{\rho T}$$

The 17 independent variables are:

$$F, P_\infty, P_j, \rho_\infty, \rho_j, T_\infty, T_j, U_\infty, U_j, \gamma_\infty, \gamma_j, \mu_\infty, \mu_j, A_{forebody}, A_j, \theta, \alpha$$

The variables above consist of four dimensional quantities ($mass$, $time$, $length$, $temperature$) and the dimensions of each of the variables are expressed below:

$$F = [\frac{mass * length}{time^2}]$$

$$P = [\frac{mass}{length * time^2}]$$

$$\rho = \left[\frac{mass}{length^3}\right]$$

$$T = [\ temperature\ ]$$

$$U = [\frac{length}{time}]$$

$$\gamma = [\ ]$$

$$\mu = [\frac{mass}{length * time}]$$

$$A = [\ length^2\ ]$$

$$\theta = [rad]$$

$$\alpha = [rad]$$

Using Buckingham Pi Theorem, considering that there are 17 independent dimensional variables with 4 dimensions, there are 13 non-dimensional parameters that govern the flow field.

These non-dimensional parameters are representative of the relationship between flow properties of the freestream and jet, nozzle configuration and vehicle geometry. This thesis will propose the set of these parameters believed to be the best choices due to the significance of what they describe.

To begin, the heat capacity ratios of the jet and freestream fluids ($\gamma_j, \gamma_\infty$), and also the nozzle divergence angle ($\theta$) and nozzle angle of attack ($\alpha$), measured in radians, are already non-dimensional.

Subsequently, the Mach numbers ($M_j, M_\infty$) and Reynolds numbers ($Re_j, Re_\infty$) of the two opposing flows are also thought to be influential.

$$M = \frac{U}{\sqrt{\gamma\, R\, T}} \;\; \& \;\; Re = \frac{U\sqrt{A}}{\mu/\rho}$$

Then, there is the total axial force coefficient where the total axial force is normalized:

$$C_F = \frac{F}{\frac{1}{2}\rho_\infty U_\infty^2\, A_{forebody}}$$

While the 9 aforementioned parameters are easily identified, there are 4 non-dimensional parameters left to choose.

Let's consider the variables from the control volume analysis of the thrust coefficient ($C_\Psi$) and further simplify them to determine the fundamental parameters the thrust coefficient is dependent on.

Firstly, note that the area and pressure ratios between the jet throat and exit are functions of the jet exit Mach number ($M_j$) and the heat capacity ratio ($\gamma_j$) (assuming the nozzle is isentropic) such that:

$$A_{j_{ratio}} = f(M_j, \gamma_j), \qquad P_{j_{ratio}} = g(M_j, \gamma_j)$$

Secondly, the ideal gas law and the Mach number can be used to manipulate the momentum flux ratio and the jet exit pressure coefficient such that

$$J_{flux} = \frac{U_j^2}{U_\infty^2}\,\frac{P_j}{P_\infty}\,\frac{R_j}{R_\infty}\,\frac{T_j}{T_\infty}, \qquad C_{p_j} = \frac{P_j}{P_\infty}\,\frac{2}{\gamma_\infty M_\infty^2}$$

suggesting the importance of further non-dimensional parameters which could influence the thrust coefficient. These are the squared velocity ratio, the pressure ratio, the specific gas constant ratio and the temperature ratio:

$$U_{ratio}^2 = \frac{U_j^2}{U_\infty^2}, \qquad P_{ratio} = \frac{P_j}{P_\infty}, \qquad R_{ratio} = \frac{R_j}{R_\infty}, \qquad T_{ratio} = \frac{T_j}{T_\infty}$$

Thus, thrust coefficient is equivalently rearranged to show its dependence on the following independent parameters:

$$C_\Psi = f(A_{ratio}, M_j, \gamma_j, U_{ratio}^2, P_{ratio}, R_{ratio}, T_{ratio})$$

This suggests five more potential non-dimensional variables: the area ratio, the squared velocity ratio, the pressure ratio, the specific gas constant ratio, the temperature ratio:

$$A_{ratio} = \frac{A_j}{A_{forebody}}, \qquad U_{ratio}^2 = \frac{U_j^2}{U_\infty^2}, \qquad P_{ratio} = \frac{P_j}{P_\infty}, \qquad R_{ratio} = \frac{R_j}{R_\infty}, \qquad T_{ratio} = \frac{T_j}{T_\infty}$$

Choosing the most appropriate of these parameters requires physical insights into the flow.

To begin with, bow shock properties, such as the extent of penetration, its standoff distance and unsteadiness, are important characteristics of the SRP flow field. As such, parameters that influence the bow shock are considered important.

Firstly, there is the area ratio which is known to influence the extent of bow shock penetration and bow shock unsteadiness. The forebody area is an obstacle to the flow and affects how much the flow must be deflected. As such, the area ratio between the jet and forebody represents the extent of flow deflection for a determined jet size and hence the bow shock standoff distance which determines how much momentum the jet exhaust contact surface has to penetrate the bow shock.

Secondly, the jet exit pressure coefficient from the control volume analysis was decomposed into static pressure ratio, and freestream specific heat capacity and Mach number.

$$C_{p_j} = \frac{P_j}{P_\infty} \frac{2}{\gamma_\infty M_\infty^2}$$

The demonstrates that the static pressure ratio and jet exit pressure coefficient are equivalent parameters and the static pressure was chosen as it has been shown to influence the jet expansion pattern which affects the bow shock unsteadiness.

Furthermore, freestream mass flux, which has been shown to influence the bow shock standoff distance of a blunt body (Korzun, Cordell, & Braun, 2010) is also equivalent to static pressure ratio. The freestream mass flux influences bow shocks standoff distance because more post-shock distance is required to pass higher incoming mass flux around a body. The freestream mass flux is given by,

$$\dot{m} = \rho_\infty U_\infty A_{forebody}$$

Then, using freestream properties such as pressure ($P_\infty$), velocity ($U_\infty$), forebody area ($A_{forebody}$) and dynamic pressure ($\frac{1}{2}\rho_\infty U_\infty^2$), the freestream mass flux is non-dimensionalized and normalized.

$$\frac{\frac{\dot{m}}{P_\infty}U_\infty}{A_{forebody}} = \frac{\rho_\infty U_\infty A_{forebody}}{\frac{P_\infty A_{forebody}}{U_\infty}} = \frac{\rho_\infty U_\infty^2}{P_\infty}$$

Rearranging the above parameters produces the freestream pressure coefficient:

$$C_{P_\infty} = \frac{P_\infty}{\frac{1}{2}\rho_\infty U_\infty^2}$$

This shows that the freestream mass flux is related to the freestream pressure coefficient, which means that the effects of the freestream mass flux can be demonstrated by the influence of the freestream pressure coefficient. The freestream pressure coefficient can then be further decomposed and simplified using the ideal gas law and Mach number equation such that:

$$C_{P_\infty} = \frac{2}{\gamma_\infty M_\infty^2}$$

Now recall that the jet pressure coefficient has the decomposed and simplified expression below:

$$C_{p_j} = \frac{P_j}{P_\infty}\ \frac{2}{\gamma_\infty M_\infty^2}$$

Note that the two pressure coefficients are dependent on the freestream specific heat capacity and Mach number, and they are related by the pressure ratio between the two. This means that the independent pressure parameter from the pressure coefficients is the static pressure ratio between the jet and the freestream.

However, the stagnation pressure ratio, which is more commonly used and could equivalently be chosen because Mach numbers and specific heat capacities are already parameters, is ultimately chosen instead to represent the pressure influence on the flow.

Hence, we have two parameters chosen – the area ratio between the jet and forebody and the stagnation pressure ratio between the jet and the freestream and.

$$A_{ratio} = \frac{A_j}{A_{forebody}}, \qquad P_{0_{ratio}} = \frac{P_{0_j}}{P_{0_\infty}}$$

Next, we understand that the process of information propagation in an interactive flow is dependent of the properties of the gases involved. It can be argued that the speed of sound ratio and the specific gas constant ratio between the jet and freestream are the important parameters in the flow field.

The speed of sound ($a$) of a gas is chosen because it is representative of the basic information propagation through acoustic waves. In supersonic compressible flow, the information propagation though the fluid is driven by pressure, specifically by the acoustic waves which eventually compress to form shock waves. In this way, the speed of sound, which determines the acoustic wave propagation, create a zone of influence. This can be better understood by considering the Mach cone where information can only be propagated within the cone of influence. Because the relevant Mach numbers are already considered parameters, the speed of sound ratio between the jet and the freestream is chosen because it is complementary and encompassing in representing the fundamental information propagation capability of a gas.

Secondly, the specific gas constant ($R$) of a gas is chosen because it is a physical constant that represents the relationship between other fundamental properties of the gas such as static

pressure, density and temperature. Fundamentally, the specific gas constant is related to the Boltzmann constant and is representative of the energy transfer at a molecular level. It can be also thought of as demonstrating the degrees of freedom of energy transfer. As such, the specific gas constant ratio between the jet and freestream is chosen because it represents the relationship between other fundamental properties of a gas and the process of energy transfer throughout the gas, which influences how information is propagated throughout the gas.

Hence, we have two more parameters chosen –the speed of sound ratio and specific gas constant ratio between the jet and freestream:

$$a_{ratio} = \frac{a_j}{a_\infty}, \qquad R_{ratio} = \frac{R_j}{R_\infty}$$

Note that these two ratios are independent of other parameters already chosen and are simply related to the choice of gas and its temperature.

Finally, the 12 non-dimensional numbers are

$$\gamma_j, \gamma_\infty, \theta, M_\infty, M_j, Re_j, Re_\infty, C_F = \frac{F}{\frac{1}{2}\rho_\infty U_\infty^2 \, A_{forebody}}$$

$$a_{ratio} = \frac{a_j}{a_\infty}, R_{ratio} = \frac{R_j}{R_\infty}, P_{0_{ratio}} = \frac{P_{0_j}}{P_{0_\infty}}, A_{ratio} = \frac{A_j}{A_{forebody}}$$

These non-dimensional parameters are all independent and fundamentally influence the total axial force and SRP flow field behavior. It follows that the total axial force coefficient can be expressed as a function of the following parameters

$$C_F = f(\gamma_j, \gamma_\infty, \theta, \alpha, M_\infty, M_j, Re_j, Re_\infty, a_{ratio}, R_{ratio}, P_{0_{ratio}}, A_{ratio})$$

Strong arguments have been made for the chosen parameters based on known physical phenomena, however it is clear that there are other candidates. Experimental data is required to validate these choices.

## 3.3. Choosing parameters to investigate experimentally

It is necessary to reduce the number of parameters for efficient investigation. Thus, this thesis argues for a few important parameters to be examined.

The two parameters that greatly impact flow field dynamics are the Mach numbers and Reynolds numbers of the flows, however, it is argued that the Reynolds number of the flows are relatively less important. This is because Mach number determines the big discontinuities and structures of the flow while flows require relatively substantial changes in Reynolds number to significantly influence the viscous processes under investigation. The SRP flow field interaction has relatively large changes in Mach number compared to smaller changes in Reynolds number, and the viscous effects on the shear layers in SRP flows are thought to be secondary to the large scale discontinuities experienced by the flow. Hence, the Mach numbers are more important than Reynolds number for SRP flow field interaction.

This thesis also chooses not to investigate geometric configuration parameters and gas property specific parameters. For instance, the retronozzle divergence angle is fixed ($\theta = 4.5°$) with the choice of nozzle used and the nozzle angle of attack is fixed because the nozzle points directly into the oncoming flow ($\alpha = 0$). Also, the area ratio is also fixed at unity ($A_{ratio} = 1$) due to our geometrical configuration selection of no forebody. Furthermore, identical gases are chosen for the freestream and jet flows which fix the specific heat capacities and specific gas constant ratio.

Therefore, this leaves us with a few select important parameters to investigate experimentally:

$$C_F = f(M_\infty, M_j, a_{ratio}, P_{0_{ratio}})$$

In our experimentation, the gases used will have the identical initial total temperature and Mach number. This determines the Mach numbers and speed of sound ratio. Note that the speed of sound ratio is a very interesting parameter to explore but is harder to do experimentally.

Finally, this thesis will only focus on investigating the stagnation pressure ratio influence on SRP flow steadiness.

# 4. Experimental Investigation

The purpose of this experimental investigation is to explore the influence of stagnation pressure ratio between the jet and freestream flow on SRP flow field behavior. The stagnation pressure ratio influences the different retronozzle jet expansion patterns that subsequently affects bow shock unsteadiness, which is used to indicate SRP flow unsteadiness.

The rest of the parameters from the dimensional analysis are kept constant for the experiments. It was chosen to examine a single nozzle configuration with no forebody ($A_{ratio} = 1$) and at zero angle of attack ($\alpha = 0$), which omits the recirculation region caused but the forebody deflection that might modulate the flow. Moreover, the resultant decrease in bow shock standoff distance will provide a more precise examination of the jet exhaust and freestream flow interaction. Also, the gases for the freestream and retronozzle jet flows are chosen to be Nitrogen at Mach 2. This fixes the specific gas constant ratio ($R_{ratio} = 1$), the specific heat capacities ($\gamma_j, \gamma_\infty = 1.4$), the Mach numbers ($M_j, M_\infty = 2$) and Reynolds numbers ($Re_j, Re_\infty \approx 1600$) of the flows and the speed of sound ratio ($a_{ratio} = 1$) between the flows. Also, the retronozzle is conical with a constant divergence angle ($\theta = 4.5$) for ease of manufacturing.

## 4.1. Facilities and Methods

### 4.1.1. Supersonic Wind Tunnel

A Ludwieg Tube was used as a cost effective and easily customizable set up that produces supersonic flow for short periods of time. This is achieved by attaching a convergent-divergent nozzle at the downstream end and with the upstream section being closed which acts as the pressurized storage tank.

For the experiment, a $10\ ft$ Ludwieg Tube was used and pressurized before a triggered venting, using a system of two diaphragms at the ends of a $3.5\ in$ breach section, pushes subsonic flow

through a Mach 2 supersonic nozzle which produces $0.63s$ of supersonic flow. The choice of the two-diaphragm system allows better control over the final discharge stagnation pressure of the Ludwieg Tube before burst.

In this set up, the upstream diaphragm closed off the section of the Ludwieg Tube that is pressurized to the desired discharge stagnation pressure. Then, the section between the two diaphragms is vented to trigger the upstream diaphragm to burst first before triggering the downstream diaphragm to burst. Figure 9, a simplified x-t diagram for a single diaphragm Ludwieg Tube set up, shows the characteristic wave propagations when the upstream diaphragm bursts.

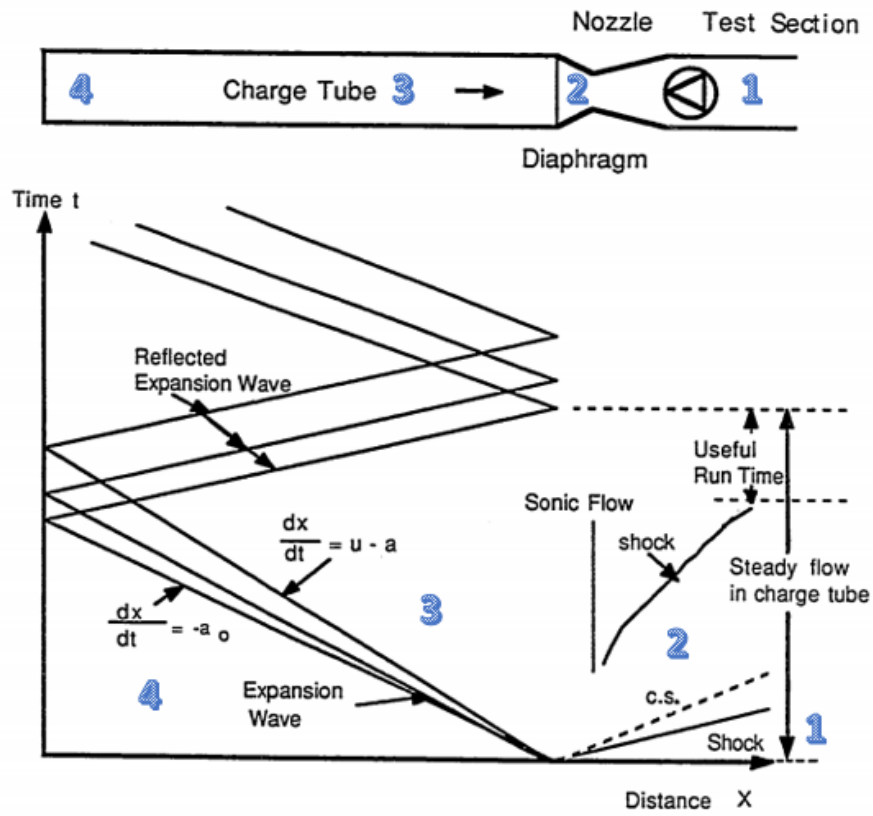


**Figure 9: Ludwieg Tube x-t diagram (Wang, 1989)**

When the diaphragm bursts, a shock wave propagates downstream through region 2 (nozzle section) and into region 1 (open air test section), which produces supersonic flow. At the same time, an unsteady expansion wave propagates upstream into region 4 (the pressurized Ludwieg Tube section). This expansion wave is eventually reflected off the closed end of the Ludwieg Tube as a compression wave into region 3. When the compression wave reaches region 2, part of it continues through as a compression wave into region 1 while part of it is reflected back into region 3 as an expansion wave. The complete wave propagation from region 2 to region 4 and back is distinguished as a Ludwieg Tube flow 'cycle'. The subsequent flow cycles decrease in driving stagnation pressure and eventually the Ludwieg Tube is vented.

The right diagram shows some pressure and temperature trends used to approximate Ludwieg Tube quantities due to pressure losses, these equations will be used to approximate the Ludwieg Tube discharge pressure approximation.

Ludwieg Tube discharge pressure approximation

For the experiment, the Ludwieg Tube is being fired into open air at ambient room pressure. From Figure 9, only the first cycle of the Ludwieg tube is useful for the experiment and thus the discharge stagnation pressure must be accurate and specific for a perfectly expanded Mach 2 flow. This is achieved by using equations (Wang, 1989) that account for the Ludweig Tube property trends shown in Figure 10. Note that the subscript 's' corresponds to region 4 of the Ludwieg Tube.

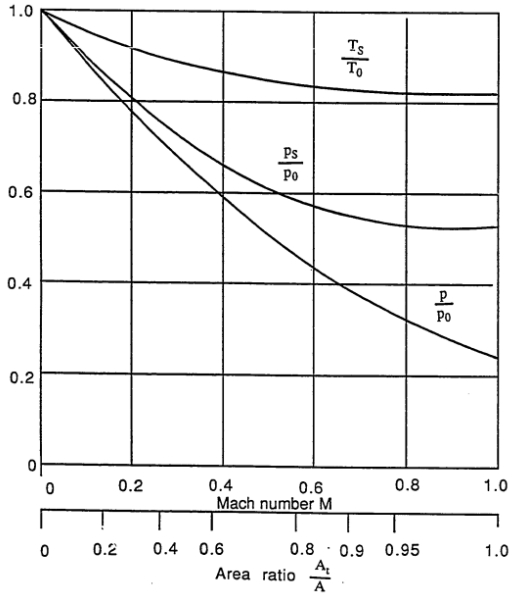


**Figure 10: Pressure and Temperature ratio trends (Wang, 1989)**

First, the area ratio between the Ludwieg Tube ($A_4$) and the nozzle throat ($A^*$) expressed as a function of the flow Mach number before the nozzle ($M_2$).

$$\frac{A_4}{A^*} = \frac{1}{M_2}\left[\frac{1+\frac{\gamma-1}{2}M_2^2}{\frac{\gamma+1}{2}}\right]^{\frac{\gamma+1}{2(\gamma-1)}}$$

Since the areas are known, the Mach number of the flow upstream of the nozzle can be calculated. Note that solving this equation produces two Mach numbers – one subsonic and one supersonic. The realistic subsonic Mach number is chosen because a supersonic flow requires compression of a subsonic flow.

Then, $M_2$ is used to calculate the temperature ratio between the stagnation temperature ($T_0$) and the Ludwieg Tube ($T_4$).

$$\frac{T_0}{T_4} = \frac{1+\frac{\gamma-1}{2}M_2^2}{\left(1+\frac{\gamma-1}{2}M_2\right)^2}$$

Next, the pressure ratio between the stagnation pressure ($P_0$) and the Ludwieg Tube ($P_4$) is calculated using isentropic relations between the temperature and the pressure ratio.

$$\frac{P_0}{P_4} = \left(\frac{T_0}{T_4}\right)^{\frac{\gamma}{\gamma-1}}$$

To calculate the stagnation pressure ($P_0$) of the flow, the pressure ratio between static and stagnation pressure from isentropic relations for a Mach 2 flow is used with the static pressure is the atmospheric pressure ($P_{atm}$). Note that this stagnation pressure is specific only to the experiment set up of this thesis because the Ludwieg Tube is being fired into open air at ambient room pressure.

$$\frac{P_{static}}{P_0} = 0.1278\ (for\ Mach\ 2\ flow)$$

$$P_0 = \frac{P_{atm}}{\frac{P_{static}}{P_0}}$$

Finally, the driving stagnation pressure of the Ludwieg tube for the experiement is calculated.

$$P_{L.T.} = \frac{P_0}{\frac{P_0}{P_{L.T.}}} = 140\ psi$$

It was found during experiments that at this discharge stagnation pressure, the first cycle of the Ludwieg Tube flow was approximately perfectly expanded and fit for use. The remaining waves present in the flow are thought to be due to viscous effects in the nozzle which effectively cause imperfect geometry.

Diaphragms

The circular diaphragms were made with $4\ mil$ Mylar material and $5.8\ inches$ in diameter. Through experimental testing, it was found that the burst pressure of the diaphragms, which is the pressure difference across the diaphragm necessary for bursting it, is $115\ psi$.

Supersonic Nozzle Design (Freestream and Retronozzle)

The method of characteristics was used to design the axisymmetric Mach 2 supersonic nozzles used in the experiment. The first nozzle is a convergent-divergent nozzle for the Ludwieg Tube which produced the freestream supersonic flow and the second nozzle is a conical nozzle, with divergence angle $\theta = 4.5°$, for the retro supersonic flow. The freestream flow nozzle is $2\ in$ in diameter while the retro flow nozzle is $0.235\ in$ in diameter. The CAD models for the supersonic nozzles are shown in Figure 11.

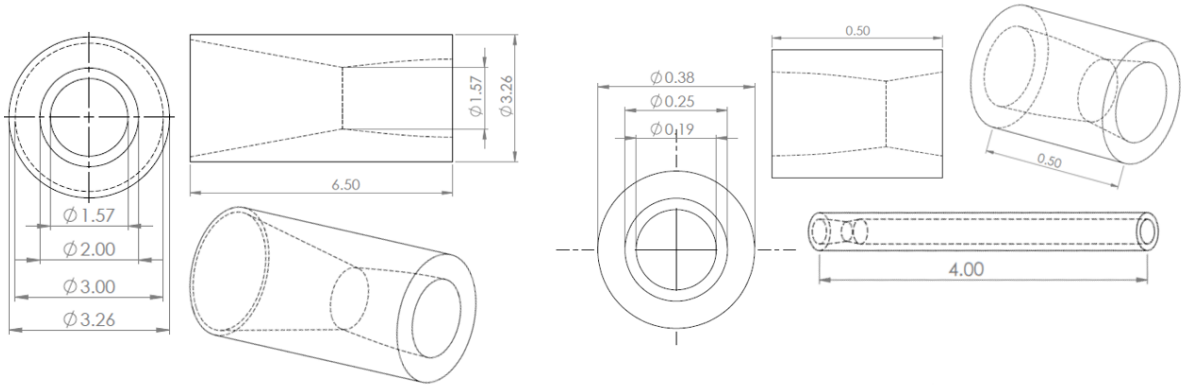


**Figure 11: (left) Freestream flow nozzle ; (right) Retro flow nozzle**

### 4.1.2. Schlieren Photography

Flow visualization data is collected using schlieren Photography. In the experiment, a concave converging mirror is used, which is shown in Figure 12.

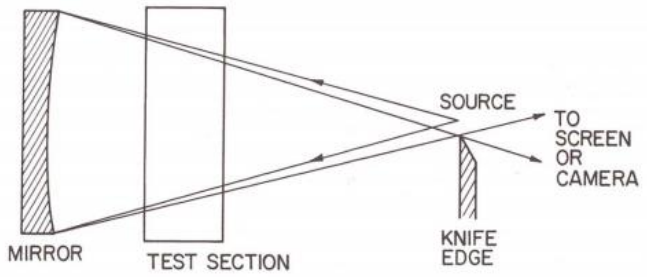


**Figure 12: Modified schlieren photography set up (Hu, n.d.)**

The light travels from the light source, is reflected off the mirror and through the test medium. A knife edge is placed at the focal point of the reflected light rays and positioned to block the light. For images with density variations, the distorted light rays focus differently on the screen or camera. This results in lighter and darker patches in the image that corresponds to positive and negative density gradients. In this way, schlieren photography measures the first derivative of the index of refraction and the amount of light blocked is related to the sensitivity of the schlieren. These density gradients are in the direction normal to the knife edge. As such, this experiment has a vertical razor cut off, so we look at gradients in the horizontal direction, longitudinal to the SRP flow interaction.

In the experiment, the schlieren is set up following a baseline reference configuration, as seen in Figure 13, and small adjustments are made. These include focusing the camera on the plane of the retronozzle, using a constant razor cutoff and increasing or decreasing the aperture.

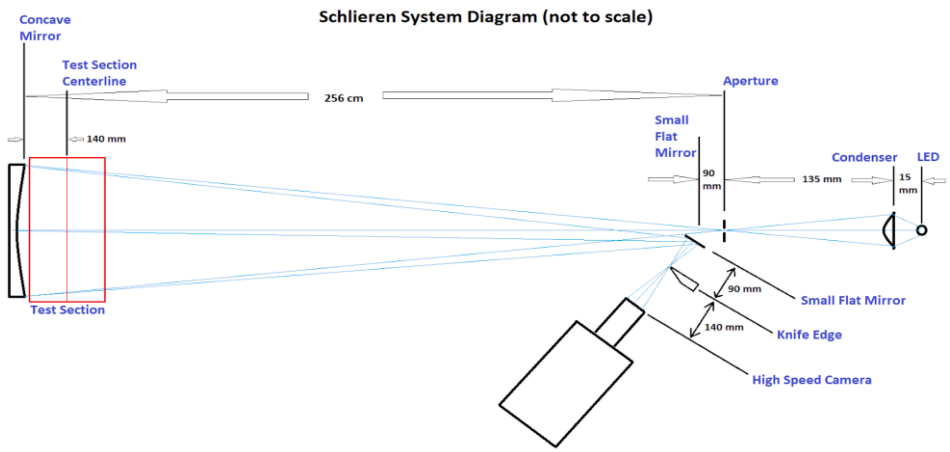


**Figure 13: Experimental schlieren set up baseline configuration**

The razor cutoff is fixed using a polarizer in the image and adjusting the cutoff based on the darkness of the polarizer (Settles, 1949). This is because the angle between the polarizer and the mirror is proportional to the refraction angle, which is the angle that reflects the distance of the extent of light refraction in the medium. Hence, by using the same angle between the polarizer and mirror, we can adjust the razor cutoff to be the constant. The aperture is then adjusted to produce an 8-bit image greyscale value of about 130 for the bright background.

Image Capture

The schlieren photography was captured using the Phantom Vision Research v1211 camera funded by the Student Technology Fee from the University of Washington. The camera was used with a lens at maximum aperture and $300mm$ focal length. Other camera settings, such as the frame rate and exposure time for the videos, are shown in Table 1.

| Setting | Value |
|---|---|
| Resolution | $512\ pixels \times 512\ pixels$ |
| Frames Per Second | 37,000 |
| Exposure Time | $8\ \mu s$ |

**Table 1: Phantom v1211 camera settings used.**

## 4.2. Test Conditions

For the scope of this thesis, only stagnation pressure ratio between the freestream and retronozzle jet flow ($P_0$ ratio $= P_{0_j}/P_{0_\infty}$) was varied. The retronozzle jet stagnation pressures ($P_{0_j}$) were determined using the isentropic relations for a Mach 2 flow. The various $P_{0_j}/P_{0_\infty}$ values and the corresponding $P_{0_j}$ values are shown in Table 2.

| $P_{0_j}/P_{0_\infty}\ ratio$ | $P_{0_j}\ [psi]$ |
|---|---|
| 0 | 0 |
| 0.5 | 57.5 |
| 0.75 | 86.25 |
| 1 | 115 |
| 2 | 230 |
| 3 | 345 |
| 4 | 460 |
| 5 | 575 |

**Table 2: Experimental Test Conditions for varying $P_{0_j}/P_{0_\infty}$ ratio**

The first case without the retronozzle jet operational is a control case while the subsequent cases vary the retronozzle jet expansion.

## 4.3. Safety Calculations

To ensure a safe experiment, calculations were made to guarantee that the apparatus was rated for the high pressures we would be operating at.

First, hoop stress calculations, with thin-wall approximation, were calculated for the Ludwieg Tube, freestream supersonic nozzle throat and exit and the supersonic retronozzle jet. The Ludwieg Tube and freestream nozzle estimated failure pressures were calculated with the Ludwieg Tube discharge stagnation pressure ratio while the retronozzle jet estimated failure pressure was calculated with the highest operational pressure for $P_{0_j}/P_{0_\infty} = 5$. These calculated values are shown in Table 3.

| **Apparatus** | **Estimated Failure Pressure [$psi$]** |
|---|---|
| Ludwieg Tube | 7196 |
| Freestream Nozzle – throat | 25,606 |
| Freestream Nozzle – exit | 18,409 |
| Retronozzle Jet | 3100 |

**Table 3: Estimated Failure Pressures for Apparatus**

Secondly, thread calculations were also done and found that a minimum thread engagement length of $.125\ in$ was necessary for retronozzle and Ludwieg Tube plumbing set up, which meant that connections provided at least a factor of safety of 6.

## 4.4. Experimental challenges

There following are a few anticipated issues with the experimental set up that have been corrected for as best as possible but still should be noted.

The schlieren was too sensitive and could be reduced for future experimentations. For the choice of schlieren set up, schlieren sensitivity is proportional to the focal length of the concave mirror used and inversely proportional to the amount of razor cutoff. Since the focal length of our mirror is relatively far, our schlieren is very sensitive. This means that slight changes in the

density gradients are very pronounced. This is further exaggerated by the vibration of the mirror during the experiment testing due to the proximity of its placement to the flow. To reduce the ‘noise’ of the data, video frames will be normalized to average out the overall image illumination.

Also, it was noted that the mirror used in the schlieren set up vibrated quite a lot initially when the flow interaction began. This caused the initial frames of the video to darken significantly. These frames will be cut out of the analysis.

Moreover, the retronozzle jet was secured but slight vertical movement was still observed during the experiments as it was being impinged upon by the freestream flow. In the future, trials can be done to further reduce the distance between the retronozzle jet exit and the mounting apparatus to reduce the moment arm and deflection. The reason for some distance between the retronozzle jet and the mounting is so the mounting apparatus does not interact with the flow or affect the bow shock standoff distance.

## 4.5. Data Acquisition and Processing

The raw schlieren video files were processed before analysis was conducted. Note that the raw schlieren files were collected in ‘.cine’ format (the video format for Phantom Vision Cameras) and were eventually converted to ‘uncompressed .avi’ format before using MATLAB software for image analysis.

The video files are trimmed to the time for only the first flow cycle of the Ludwig Tube and cropped to the resolution focused on the actual interaction zone between the two flows. Specifically, the frame analyzed focuses only on the flow within the freestream flow to simulate the type of data obtained from a wind tunnel facility.

Videos were then normalized due to disturbances caused by the schlieren set. This was achieved by finding the average intensity of the entire frame and repeating for all the frames and all the test cases. The average intensity for all the frames across all test cases was found and each pixel from a frame was then normalized with the ratio between the total average across all test cases and frames and that frame's average intensity:

$$Normalisation = pixel \times \frac{average\ intensity\ of\ all\ frames\ and\ all\ test\ cases}{average\ intensity\ of\ frames}$$

The process of normalization resulted in further trimming of the video frames due to the noise present in the initial video frames from the mirror vibration.

Finally, a total of 424 frames were used for image processing of each case.

# 5. Results and Discussion

## 5.1. Data collection and preliminary processing

The following images in Figure 14 illustrate instantaneous images of the retronozzle jet expansion pattern and SRP flow across $P_{0_j}/P_{0_\infty}$ ratios of the experiment test cases.

$\frac{P_{0_j}}{P_{0_\infty}} = 0$

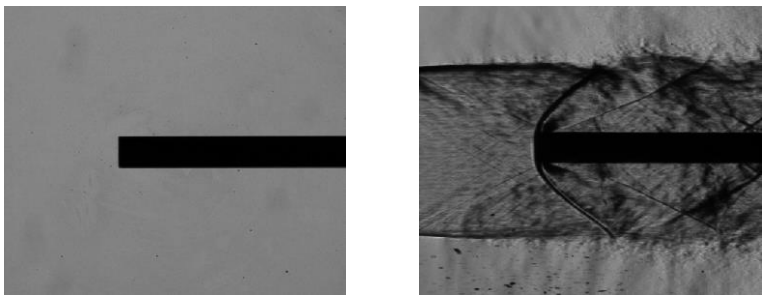

$\frac{P_{0_j}}{P_{0_\infty}} = 0.5$

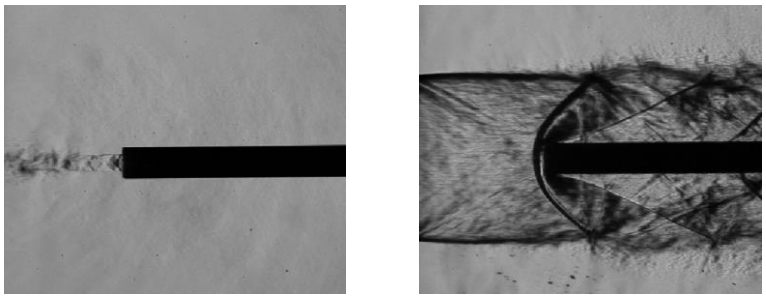

$\frac{P_{0_j}}{P_{0_\infty}} = 0.75$

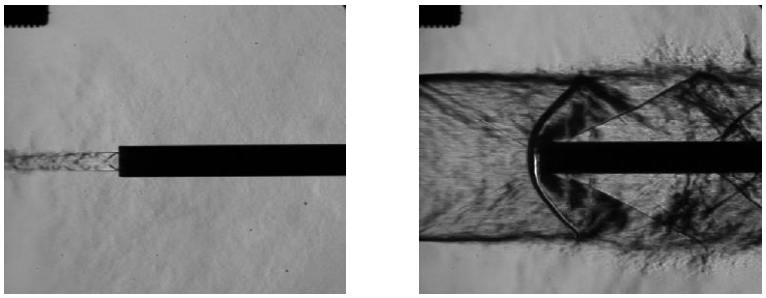

$\frac{P_{0_j}}{P_{0_\infty}} = 1$

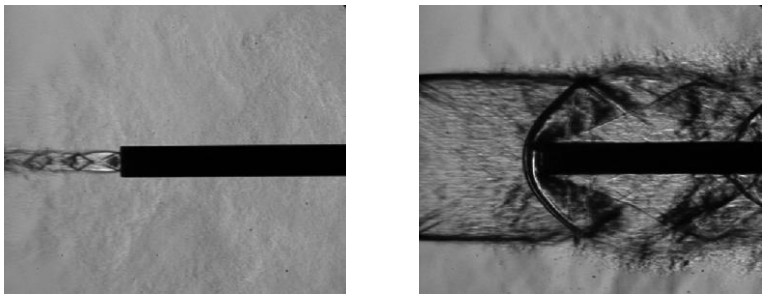

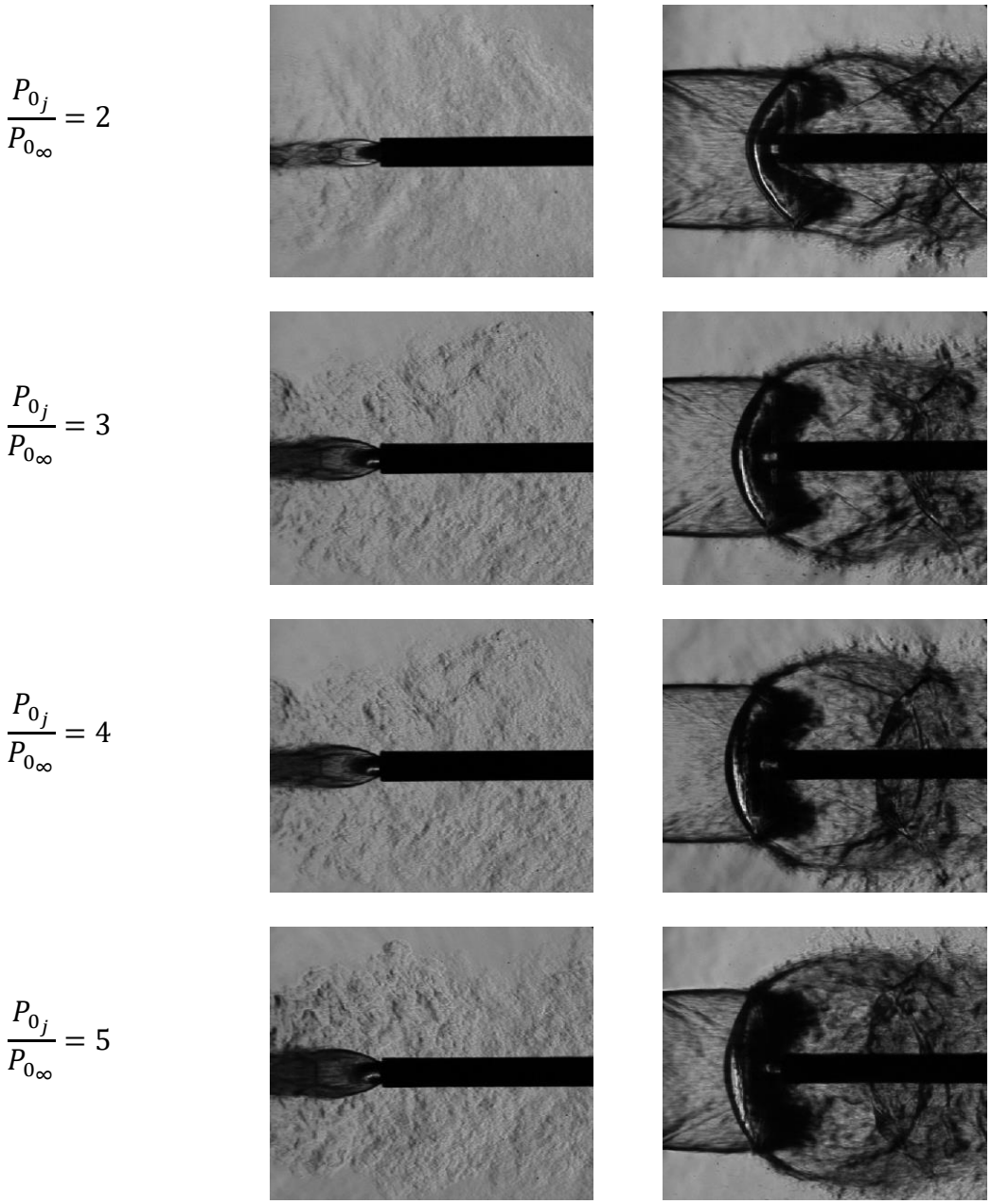


**Figure 14: Instantaneous images of (left) Retronozzle Jet Expansion, (right) SRP still image**

As expected, the retronozzle jet transitions between over-expanded at $P_{0_j}/P_{0_\infty}$ ratios below unity, to moderately under-expanded at $P_{0_j}/P_{0_\infty}$ ratios about unity and finally highly under-expanded at $P_{0_j}/P_{0_\infty}$ ratios above unity. Note that because the schlieren images represent a two-dimensional view of the depth-integrated flow field, saturation in the image is attributed to dense three-

dimensional structure and motion. This is observed as the region surround the bow shock for test cases of higher $P_{0_j}/P_{0_\infty}$ ratios have much less small-structure fine detail.

The following images in Figure 15 show the processed mean and rms images of each experimental test case using the normalized videos. The mean image represents the integrated flow across time while the rms image depicts regions of greatest flow change in illumination.

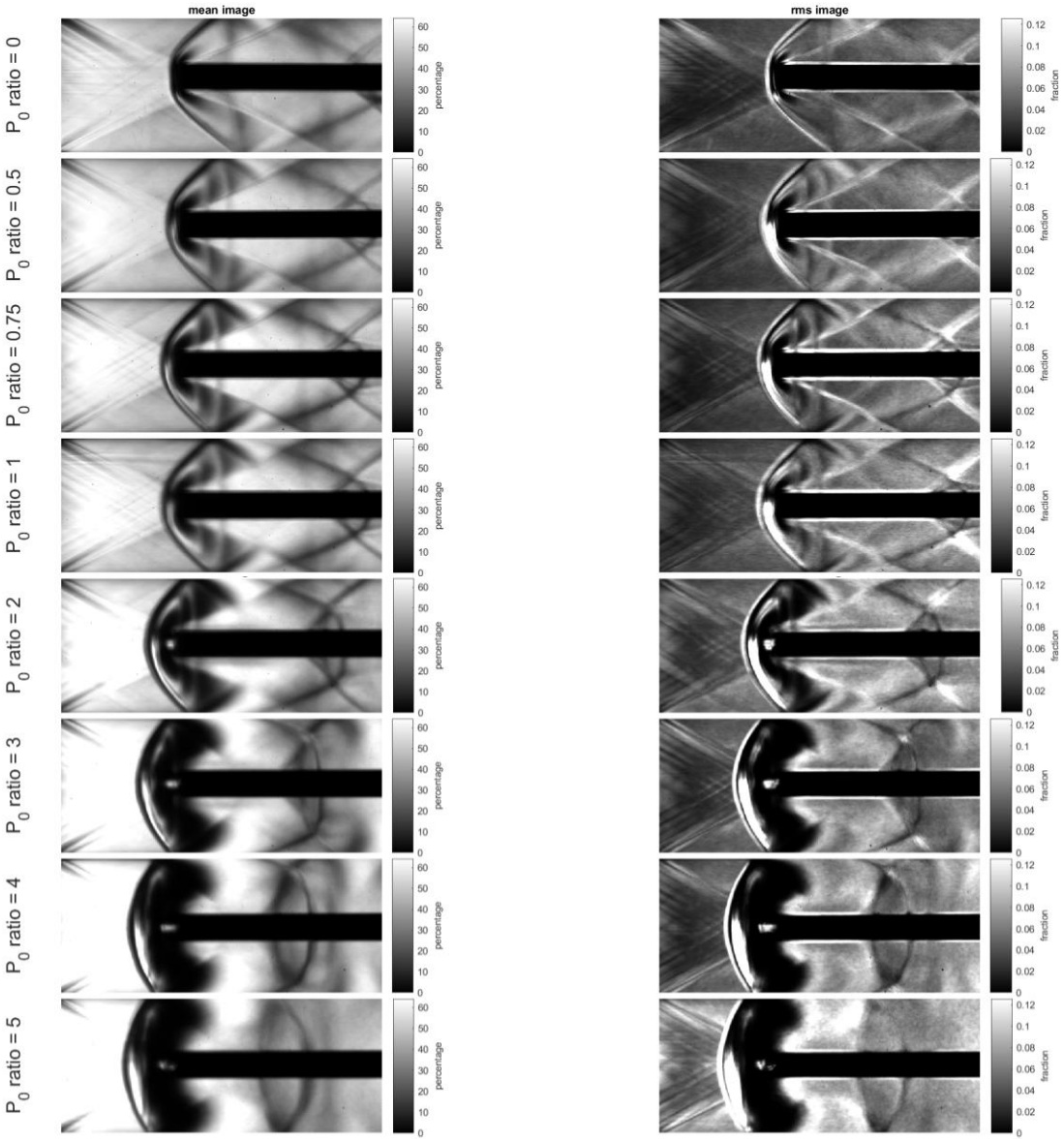


**Figure 15: The (left) mean image and (right) RMS image of SRP flow field across $P_{0_j}/P_{0_\infty}$ ratios**

From these images, key features of this SRP flow can be identified, including the bow shock between the freestream and retronozzle jet interaction and the wake downstream of the freestream after the bow shock.

Also, there are density boundaries, likely shocks or expansion waves, that separate different sections within the wake zone. The first density boundary originates from the edge of the retronozzle jet exit as a result of impingement, then it reflects off the pressure boundary between the freestream flow and atmosphere before it reflects off the retronozzle jet. Both the wake and density boundaries are evidence for a pressure gradient mismatch across the flow. As $P_{0_j}/P_{0_\infty}$ ratio increases, the greater pressure mismatch causes the reflected shocks to be less sharp due to more interference with the wake.

## 5.2. Bow Shock Properties and Unsteadiness

Bow shock properties such as bow shock topography, oscillation frequency, standoff distance, and curvature was investigated. Also, the wake region and oblique shock pattern downstream of the freestream after the bow shock will be examined.

Bow Shock Topography

The bow shock was observed to be continuously curved in all cases, both instantaneous images and mean images. This suggests that there was little penetration of the bow shock by the retronozzle jet. This could be due to the fact that the area ratio between the jet and the forebody is crucial as the forebody increases bow shock standoff distance that emphasizes the relationship between the jet exhaust momentum at its contact surface and the extent of bow shock penetration. Even though previous experiments have proposed that LPM may cause

unsteadiness, LPM is not necessary for unsteadiness and other bow shock properties can be used to identify unsteadiness

Bow Shock Motion

The bow shock oscillatory motion was observed only for the case of stagnation pressure ratio between the retronozzle jet and freestream flow at unity ($P_{0_j}/P_{0_\infty} = 1$). This was identified by watching the flow visualization videos where and the bow shock of an unsteady SRP flow tends to oscillate. The bow shock motion is characterized by first determining the bow shock period, the time for one bow shock oscillation, and then inversing it to give its the frequency. These bow shock motion values are shown in Table 4 for the case of unity stagnation pressure ratio.

| | |
|---|---|
| **Bow Shock Time Period** | $3.51 \times 10^{-4}\ s$ |
| **Bow Shock Frequency** | $2.85 \times 10^{3}\ Hz$ |

**Table 4: Bow Shock Time Period and Frequency for $P_{0_j}/P_{0_\infty} = 1$**

Figure 16 shows the extreme streamwise positions of the bow shock. The distance between the extreme streamwise positions of the bow shock is 23% of the retronozzle diameter.

The other experimental test cases were much steadier in comparison, with movement lengths of less than 5% of the retronozzle diameter, and they have bow shock time periods an order of magnitude lower and frequencies an order of magnitude higher.

As such, the only unsteady case is for unity stagnation pressure ratio between the retronozzle jet and freestream flow. The slight oscillations in other cases may be due to slight freestream unsteadiness of turbulent in the jet, which is consistent with the higher frequency.

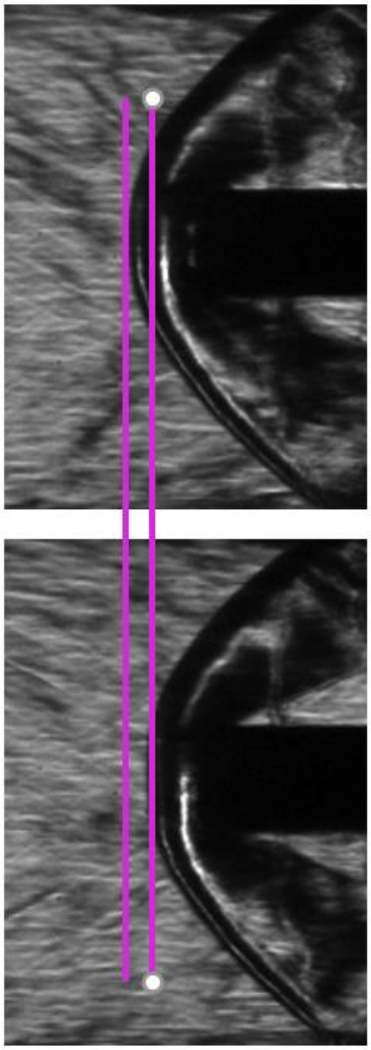

**Figure 16: Bow Shock Motion for $P_{0_j}/P_{0_\infty} = 1$**

Bow shock standoff distance

As $P_{0_j}/P_{0_\infty}$ ratio increases, the bow shock standoff distance increases as well. This trend is observed in Figure 16. The bow shock standoff distance was found by taking the average standoff distance between 25 selected frames from each test case and the error bars are the minimum and maximum standoff distance of each test case data set. Note that the standoff distance was normalized with the retronozzle diameter.

The error bars are consistent with the observation that the SRP flow for unity stagnation pressure ratio between the retronozzle jet and freestream flow is unsteady and the bow shock oscillated.

However, this result contradicts previous data that suggests that the moderately under-expanded jet with $P_{0_j}/P_{0_\infty}$ ratio around unity has the longest standoff distance, followed by the highly under-expanded jet with $P_{0_j}/P_{0_\infty}$ ratios above unity and finally the over-expanded jet with $P_{0_j}/P_{0_\infty}$ ratios under unity. This inconsistency could be due the specific geometrical configuration selection of no forebody.

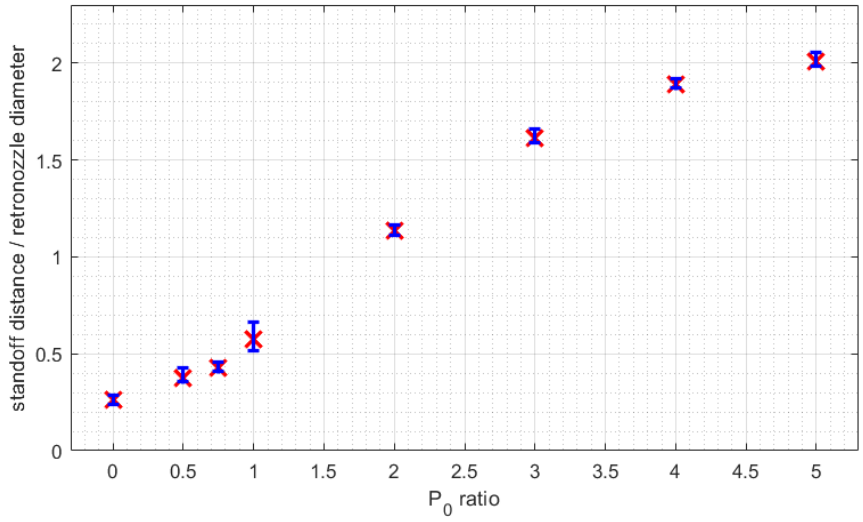


**Figure 17: Normalized Bow Shock Standoff Distance vs $P_{0_j}/P_{0_\infty}$ ratios**

Bow Shock Curvature

As $P_{0_j}/P_{0_\infty}$ ratio increases, bow shock curvature decreases. This trend is observed in Figure 17. The bow shock curvature was found by curve fitting 5 points on the bow shock of the mean image for each test case. Note that the curvature was normalized with the retronozzle diameter.

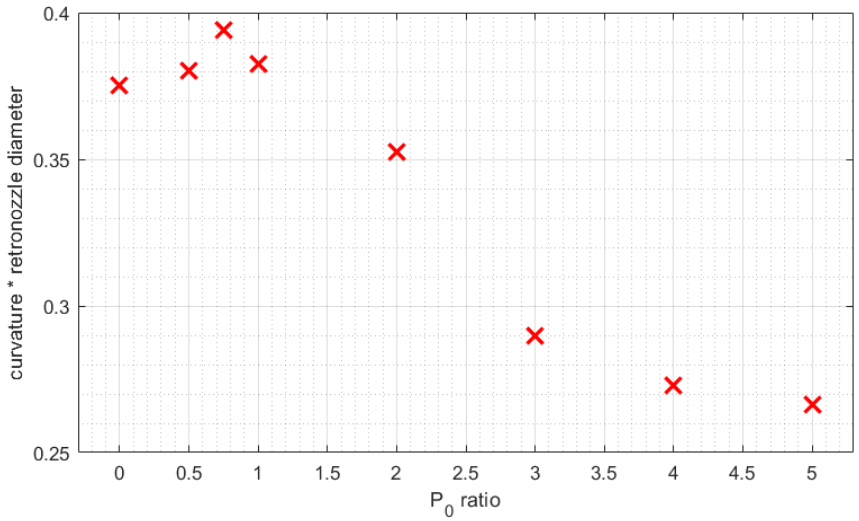


**Figure 18: Normalized Bow Shock Curvature vs $P_{0_j}/P_{0_\infty}$ ratios**

This trend can be explained by considering the effective "forebody area" of the retronozzle jet. As $P_{0_j}/P_{0_\infty}$ ratio increases, the width of the retronozzle jet increases and results in a need for increased deflection by the freestream flow. This causes the bow show to radially spread out more and become flatter. Also, there is an increased pressure gradient between the retronozzle and jet flow, which means that the bow shock must pressure match the flows further upstream.

## 5.3. Principal Component Analysis (PCA)

Principal Component Analysis (PCA) decomposes an image of the flow into a set of orthogonal modes and the linear summation of these modes and their activation coefficients, given by their singular values, reconstruct each frame. It is used for flow field behavior analysis as modes provide insight by detecting the dominant structures of the flow for that mode.

First, a data matrix ($\boldsymbol{A}$) is assembled from the normalized frames of the schlieren video in which each frame is rearranged into a column vector. As such, the data matrix for each test cases contains 424 column vectors for the 424 frames in the video and the length of each column is the number of pixels in each image.

Next, a reduced Singular Value Decomposition (SVD) is executed on the $m \times n$ data matrix to produce a set of matrices ($\widehat{\boldsymbol{U}}$, $\widehat{\boldsymbol{\Sigma}}$, and $\boldsymbol{V}^*$).

$$\boldsymbol{A} = \widehat{\boldsymbol{U}}\,\widehat{\boldsymbol{\Sigma}}\,\boldsymbol{V}^*$$

Where $\widehat{\boldsymbol{\Sigma}}$ is an $n \times n$ diagonal matrix whose elements are the singular values of the $\boldsymbol{A}$ matrix in descending order, $\boldsymbol{V}$ is an $n \times n$ unitary matrix and $\widehat{\boldsymbol{U}}$ is an $m \times n$ unitary matrix. Note that $\boldsymbol{V}$ and $\widehat{\boldsymbol{U}}$ are orthonormal and represent the bases of the $\boldsymbol{A}$ matrix. It is also important to make the distinction that $\widehat{\boldsymbol{U}}$ contains spatial information while $\boldsymbol{V}$ contains time information.

The singular values represent the weightage of each mode, which depicts the distribution of energy in the region of interest. Note that the data matrix used for analysis is the normalized data with the mean image subtracted, which is reflected with the remaining modes accounting for a lower percentage variance.

To inspect the spatial PCA modes, the columns $\widehat{\boldsymbol{U}}$ are reassembled into images. The PCA modes of the respective regions represent the fluctuations in the horizontal gradient of flow density.

This is because the schlieren photography with the vertical razor cutoff looks at the first derivative of density in the horizontal direction. Thus, the PCA modes represent the positive and negative fluctuations in image intensity, which correspond to the movement of flow structure with high density gradient. Also, note that the sign of the image intensity display is not significant as the activation coefficient can be reversed; in the PCA modes, red represents a positive density gradient while blue represents a negative density gradient, or vice versa. When one region of a mode is oppositely colored to another, this indicates that each region experiences opposite changes in image intensity when that mode is active.

### 5.3.1. Regions of Interest for PCA

There are a few regions of interest in the SRP flow interaction. PCA is performed on each separate region to allow more specific analysis of the flow structures and dynamics in that region.

First, the entire SRP flow region is analyzed. Subsequently, the region surrounding the bow shock, the wake region behind the bow shock and below the retronozzle jet, and finally the retronozzle shoulder region is all analyzed. The entire SRP flow interaction region and the individual regions are illustrated in Figure 19.

Note that for the bow shock, wake and retronozzle shoulder regions, the first mode is a uniform variation in intensity across the whole image, which suggests that it is the background disturbance mode likely caused by the mirror vibration in the schlieren set up. This mode was removed from the SRP flow region due to normalization but reappears when only a cropped region of the full frame is examined. Since this mode will disappear with the respective specific frame normalizations for all the regions, this mode will be neglected as it is an artifact of the data collection.

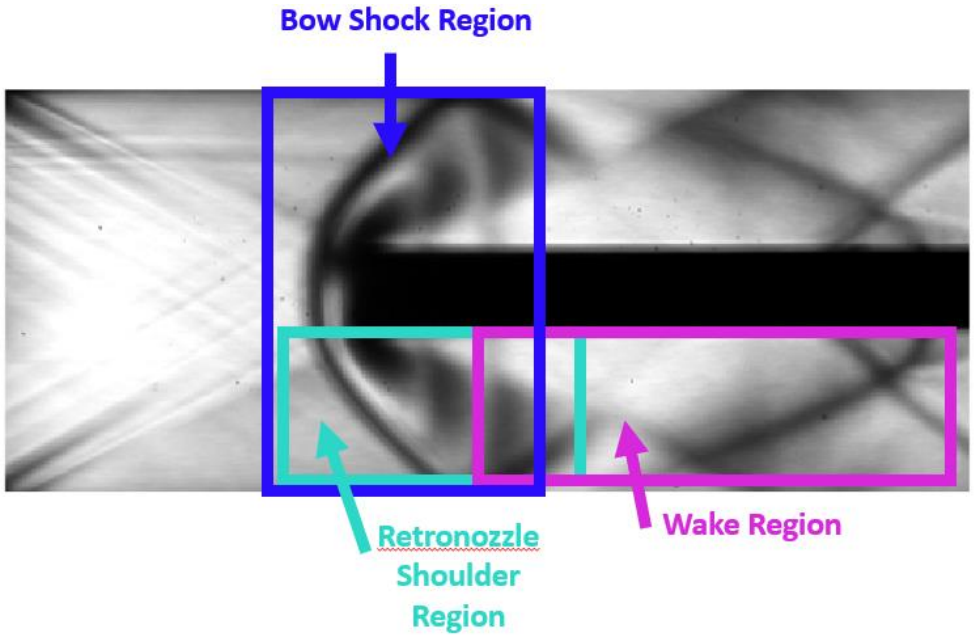


**Figure 19: Regions of Interest for PCA**

### 5.3.2. PCA Mode Interpretation

SRP Flow Region

The energy distribution of the modes are shown in Figure 20. Note that these indicate that the first principal mode only accounts for less than 2% of the image, so there is only slight broadband variation between the modes. The broadband natures means that modes are very subtle and there is no exceptionally strong unsteadines. Thus, the harmonic modes of shock motion that PCA detects are very sensitive and might not have been picked up easily by other methods of analysis.

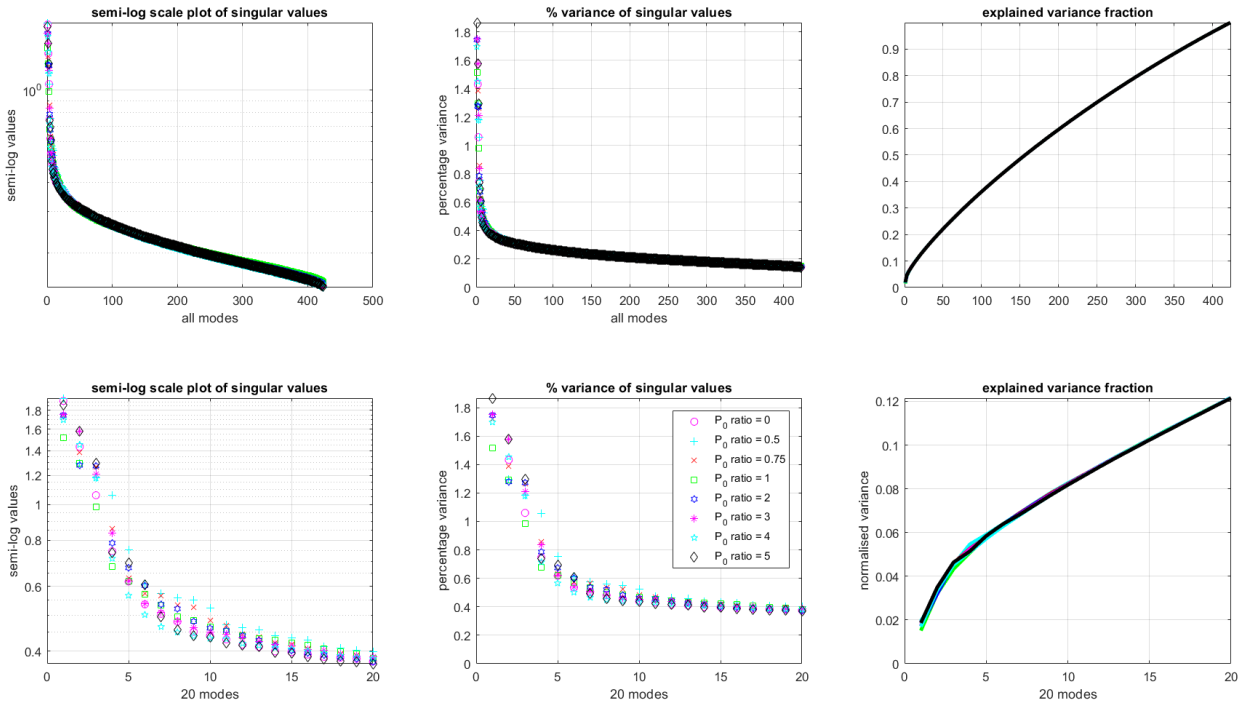


**Figure 20: Singular Values of SRP Flow Region**

PCA modes of the SRP flow region are shown in Figure 21 and 22. Figure 21 depicts the evolution of the first three modes with pressure ratio while Figure 22 depicts the evolution of the subsequent three modes with pressure ratio.

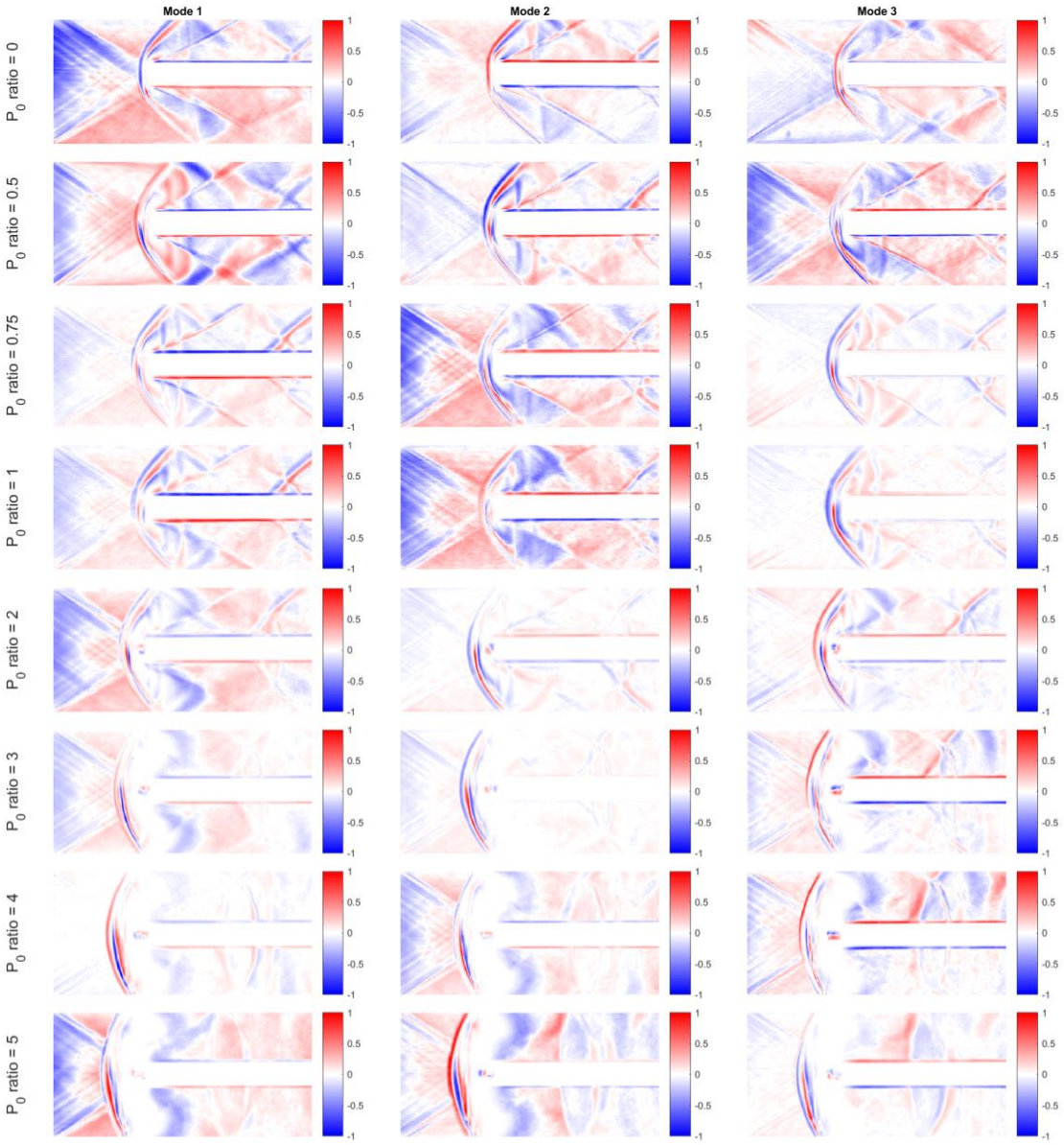


**Figure 21: SRP Flow Region PCA Modes 1-3 across $P_{0_j}/P_{0_\infty}$ ratios**

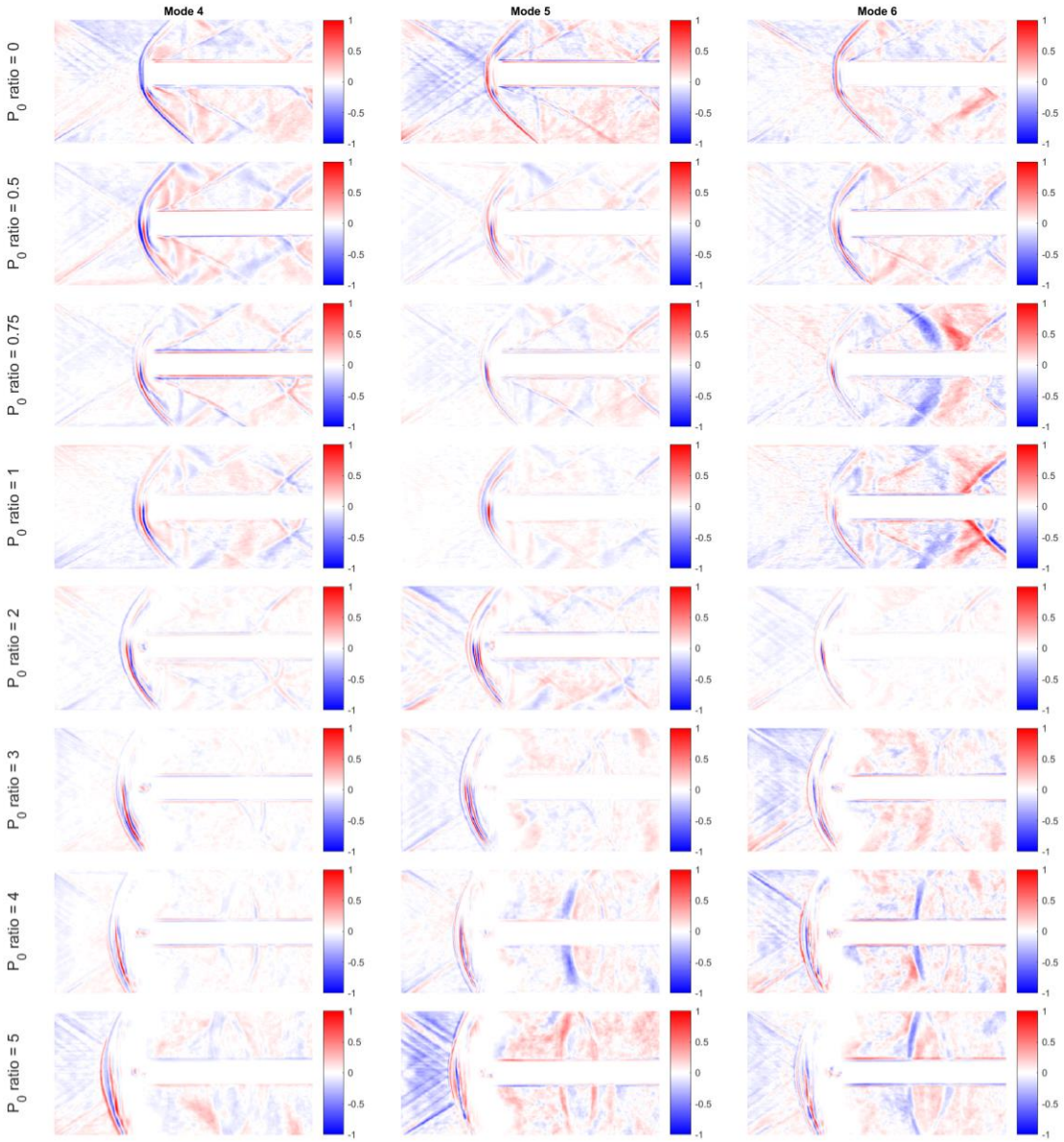


**Figure 22: SRP Flow Region PCA Modes 4-6 across $P_{0_j}/P_{0_\infty}$ ratios**

The modes above suggest some bow shock motion and wake motion. Modes are seen to highlight both the shock and expansion wave structures and the regions of the freestream. The structure upstream of the bow shock is related to the nozzle expansion of the freestream. The red and blue bands outlining the bow shock structure demonstrate the streamwise image intensity variations and represent bow shock streamwise oscillatory motion. Also, the top outline of the retronozzle and the bottom outline of the retronozzle are oppositely colored, this intensity variation represents the vertical motion of the retronozzle jet. This motion is due to the retronozzle being insecurely mounted as it is impinged upon by the freestream flow and will be neglected in analysis.

From visual inspection, the first three modes contain images of similar topography but in different order. This can be attributed to the relatively similar singular values and weightage of the modes as seen in Figure 20. The rearranged mode structures are shown in Figure 23.

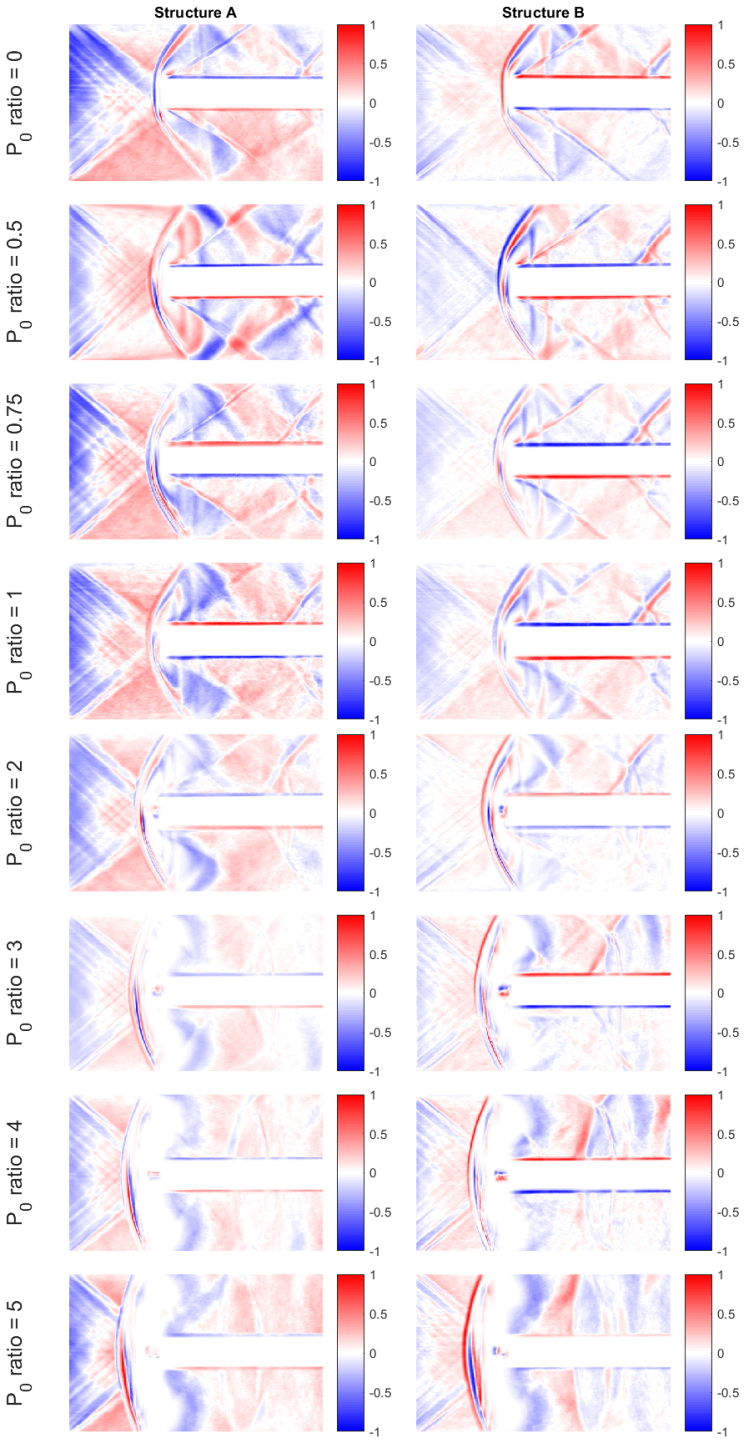


**Figure 23: SRP Flow Region PCA dominant modes across $P_{0_j}/P_{0_\infty}$ ratios**

The dominant modes of the SRP flow region in the Figure 23 demonstrate the fundamental features in the flow interaction and the motion of these structures.

First, the bow shock oscillates in the streamwise direction for all cases, even though it was only observed by eye for the single case of unity stagnation pressure ratio. The bow shock structure is outlined in alternating red and blue bands, which is the streamwise intensity variation. This suggests that the bow shock has streamwise density gradient fluctuations and can be interpreted as representing motion. Hence, the bands represent the bow shock motion harmonics.

Second, the streamwise alternating colors of the region downstream of the bow shock and surrounding the retronozzle jet show that neighboring sections have opposite changes in image intensity. Hence, this in indicative of the motion in that wake region.

From visual inspection, it seems that both Structure A and B identify features of the flow interaction downstream of the bow shock. Their color variation demonstrates how the intensity between the different regions change and is indicative of the unsteady structure motion. Structure A seems to emphasize the interaction in the vicinity of the bow shock while Structure B emphasizes the wake region downstream of the retronozzle jet exit. Particularly, Structure B appears to identify the oblique shock pattern downstream of the freestream flow behind the bow shock. It is interesting that both Structures recognize features in different regions of SRP flow.

The SRP flow field is very complicated, so subsequent cropped regions will be investigated to explore the intensity fluctuations and further support the results of my interpretation.

Bow Shock Region

The energy distribution of the modes for the bow shock region are shown in Figure 24. Note that these indicate that the first principal structural accounts for about 2.5% for the image. The low energy of the modes validates the use of PCA as such sensitive structures would not have been easily identified with other methods.

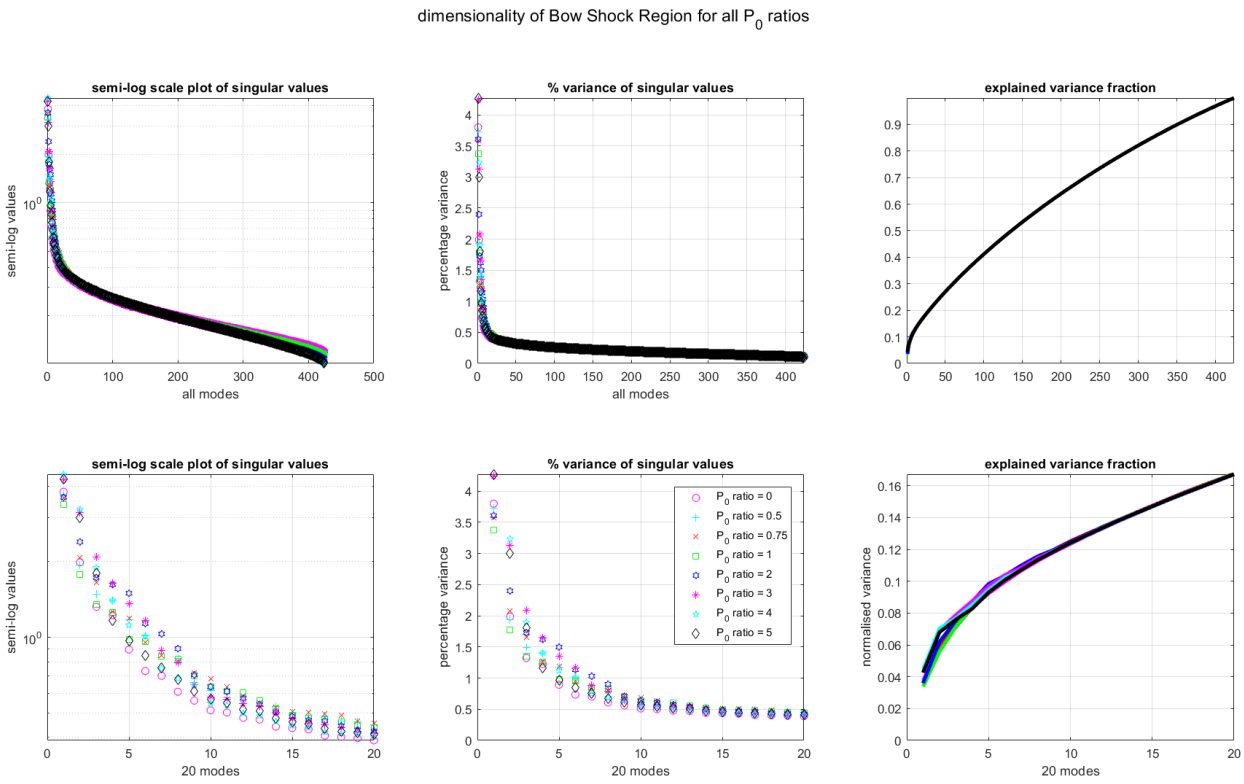


**Figure 24: Singular Values of Bow Shock Region**

PCA modes of the bow shock region are shown in Figure 25 and 26. Figure 25 depicts the evolution of the first three modes with pressure ratio while Figure 26 depicts the evolution of the subsequent three modes with pressure ratio.

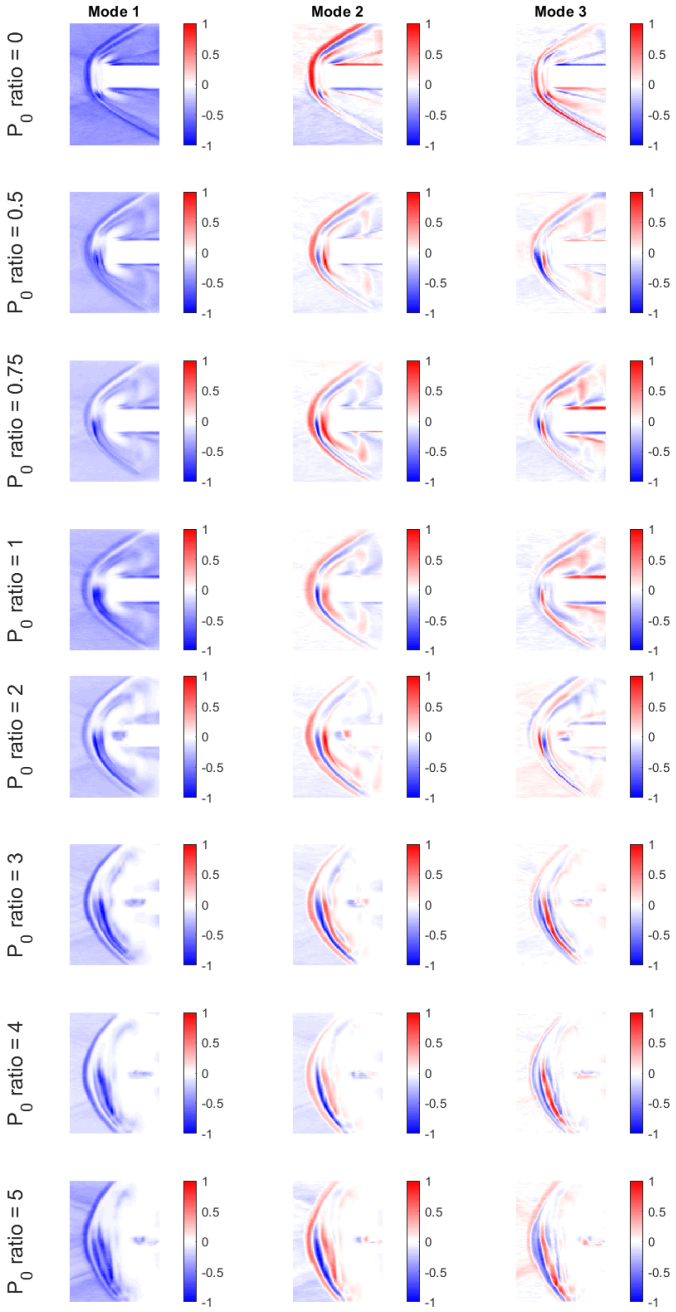


**Figure 25: Bow Shock Region PCA Modes 1-3 across $P_{0_j}/P_{0_\infty}$ ratios**

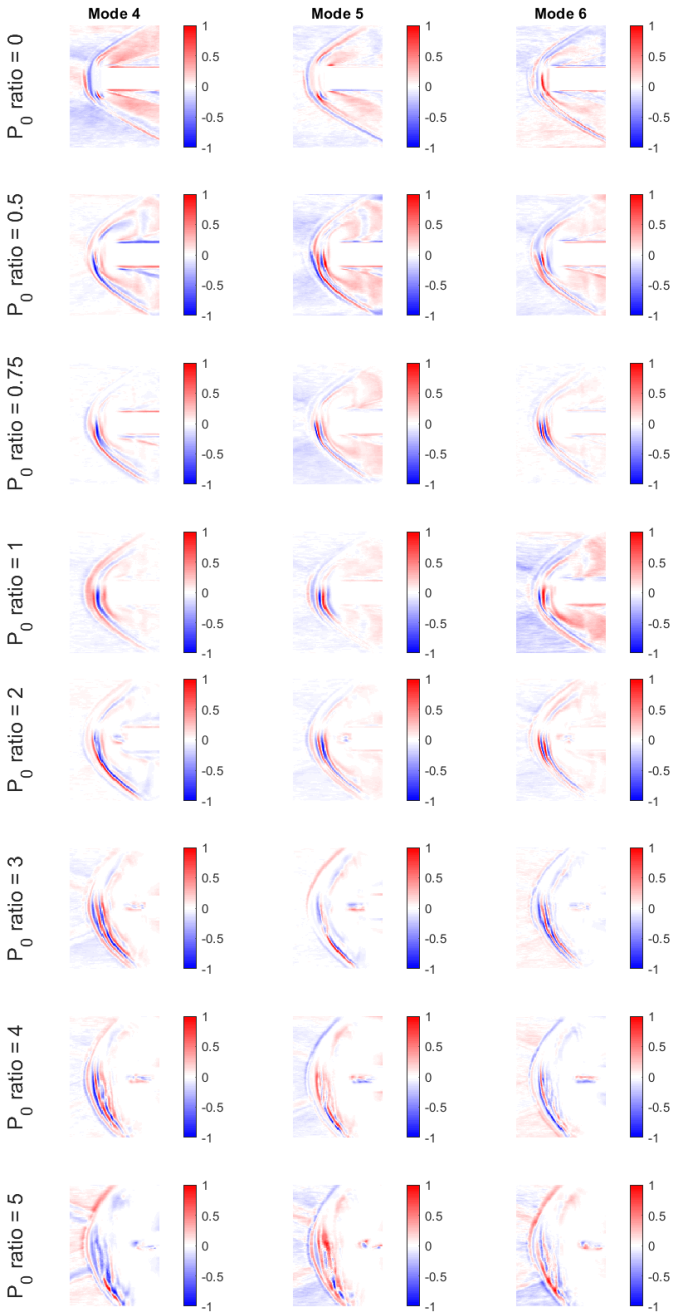


**Figure 26: Bow Shock Region PCA Modes 4-6 across $P_{0_j}/P_{0_\infty}$ ratios**

For this field of view, the motion of the bow shock motion is more easily observed.

Mode 1 in Figure 25 is uniform with a single sign and related to the mirror vibration as previously stated.

Mode 2 in Figure 25 clearly show alternating red and blue bands that outlines the bow shock position. An average of about 3 lines is observed and are approximately vertically symmetric. Subsequently, the number of bands increase in the following modes. This suggests that the modes represent the harmonics of the bow shock motion and indicate that there might be different frequencies of oscillatory motion. It is interesting to note that PCA demonstrates that all test cases have bow shock oscillatory motion and frequencies, even though it was only previously identified by eye in one test case. It is unclear from the PCA modes whether the bow shock unsteadiness is related to the upstream flow unsteadiness or cause by the SRP flow interaction.

Retronozzle Shoulder Region

The energy distribution of the modes for the retronozzle shoulder region are shown in Figure 27. The first principal structural mode accounts for about 3% of the image, which is the comparitively the highest weightage between the rest of the cropped regional modes. This suggests that the structure observed in the region is more prominent in SRP flow field behavior.

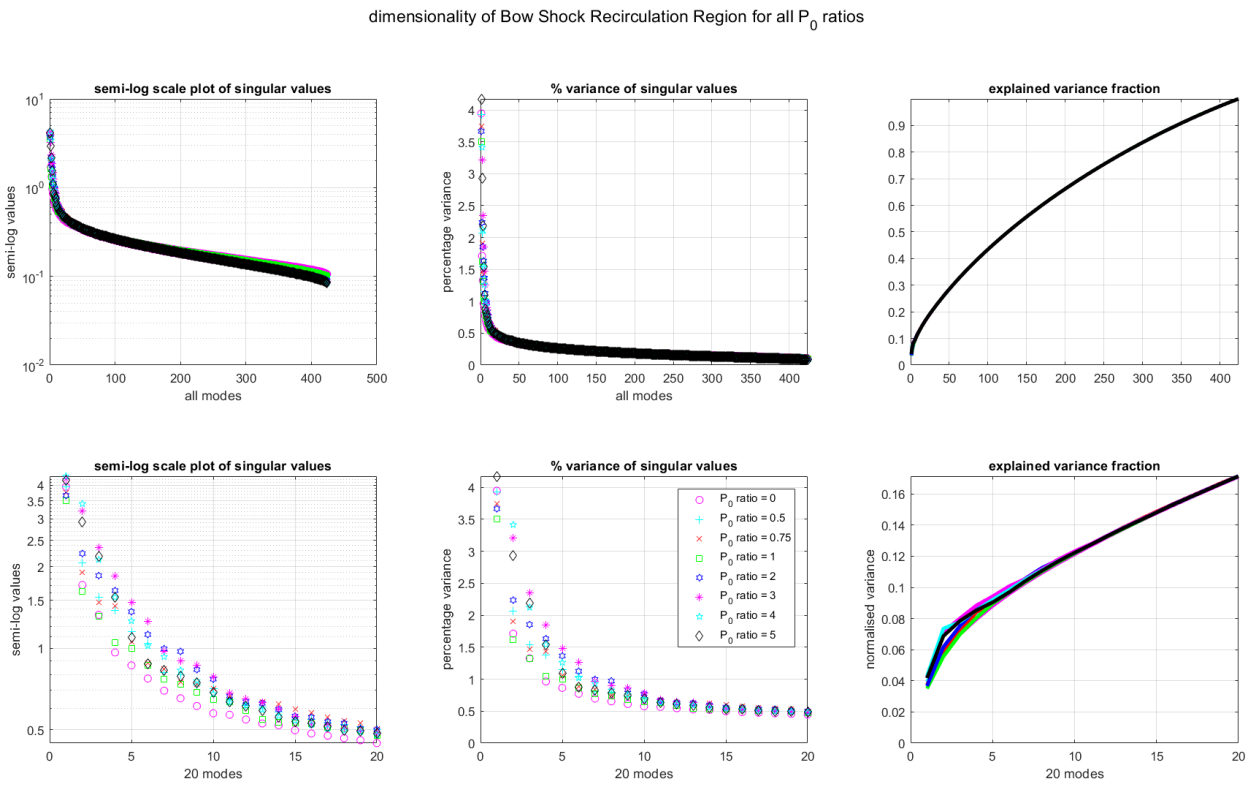


**Figure 27: Singular Values of Retronozzle Shoulder Region**

PCA modes of the retronozzle shoulder region are shown in Figure 28 and 29. Figure 28 depicts the evolution of the first three modes with pressure ratio while Figure 29 depicts the evolution of the subsequent three modes with pressure ratio.

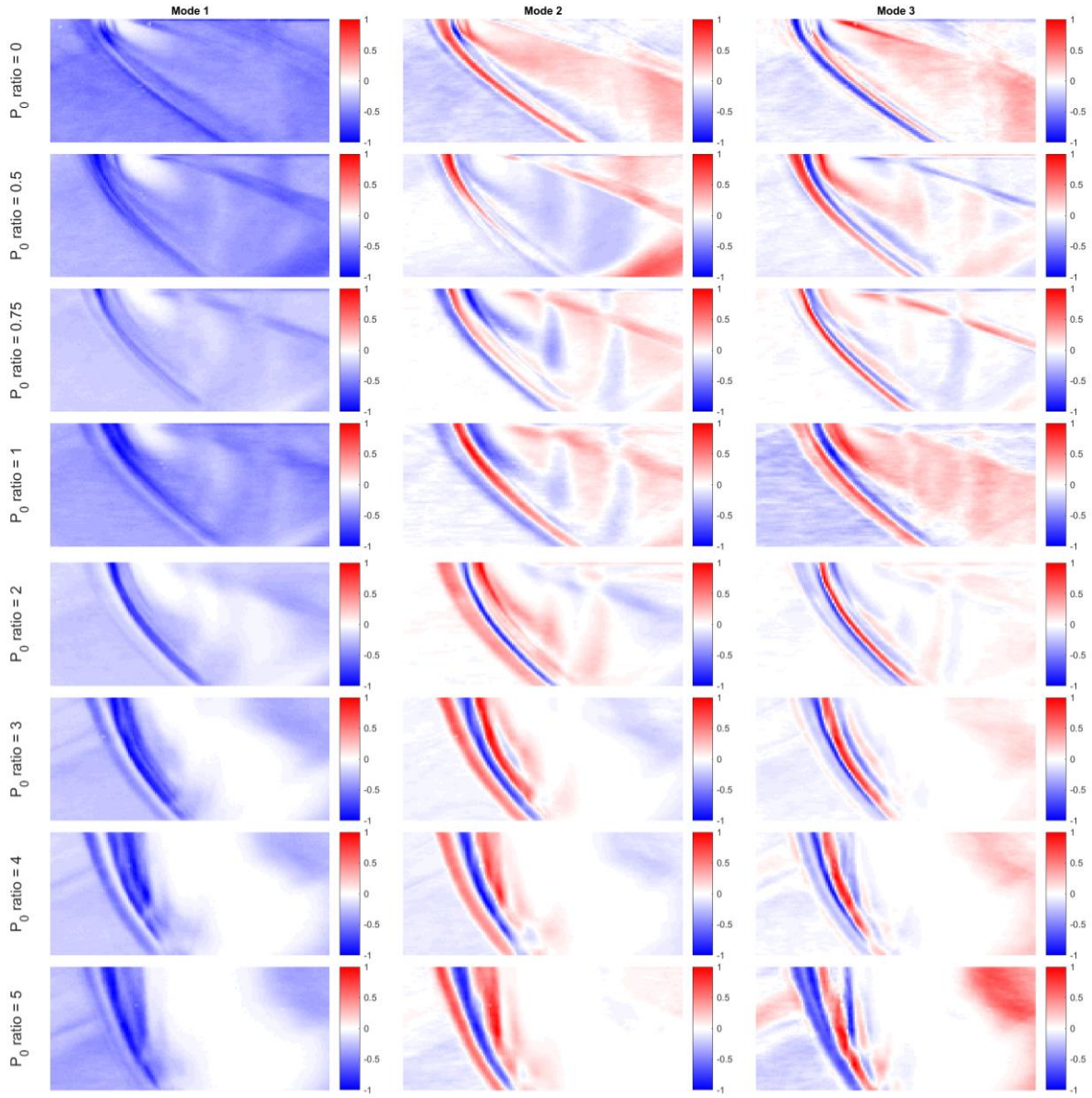


**Figure 28: Retronozzle Shoulder Region PCA Modes 1-3 across $P_{0_j}/P_{0_\infty}$ ratios**

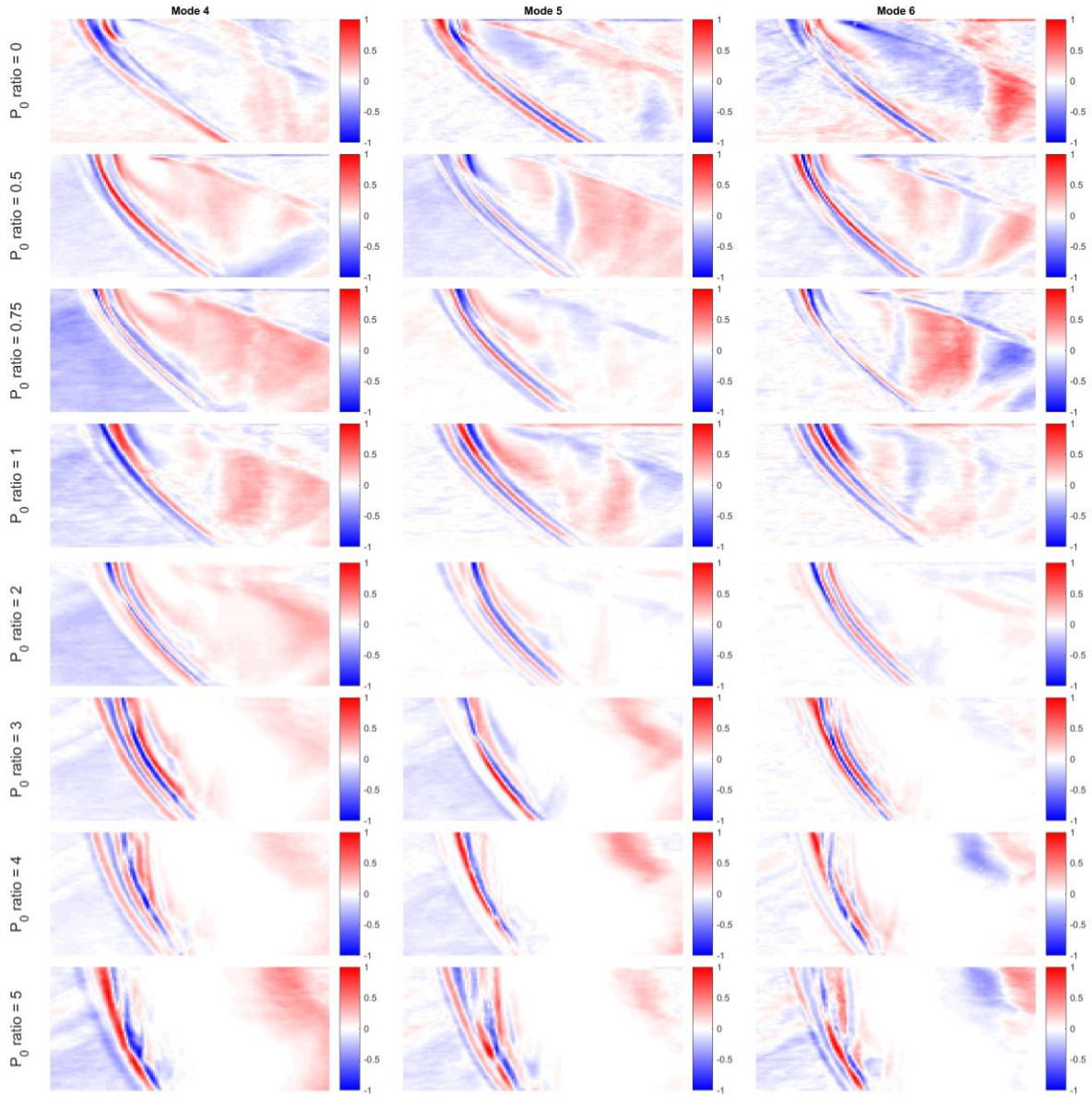


**Figure 29: Retronozzle Shoulder Region PCA Modes 4-6 across $P_{0_j}/P_{0_\infty}$ ratios**

In this region, there is clearer observation of the bow shock motion and wake region right behind the bow shock.

Mode 1 in Figure 29 is the mode related to mirror vibration, as previously mentioned.

Also, it is much clearer to observe the alternating red and blue bands of bow shock outline. In Mode 2, there are about 3 lines and the number of bands increase for the subsequent modes. This means that there are image intensity variations that indicate density gradients where the bow shock is located, which suggests bow shock motion. Moreover, the increasing number of bands in the subsequent modes suggests there are different frequencies of bow shock motion being captured in the modes. Alternatively, the different bands of color could also suggest that the bow shock topography varies as the bow shock wrinkles during oscillation.

There is not much clear structure observed in the wake region directly behind of the bow shock. Although this region becomes more saturated for increasing $P_{0_j}/P_{0_\infty}$ ratios, which may be related to the increased strength of the bow shock that saturates the schlieren image.

Wake Region

The energy distribution of the modes for the wake region are shown in Figure 30. Likewise, the first principal structural mode accounts for about 1.5% of the image, which suggests that the structures of the wake region are much more sensitive comapred to structures of previous regioins anlyzed.

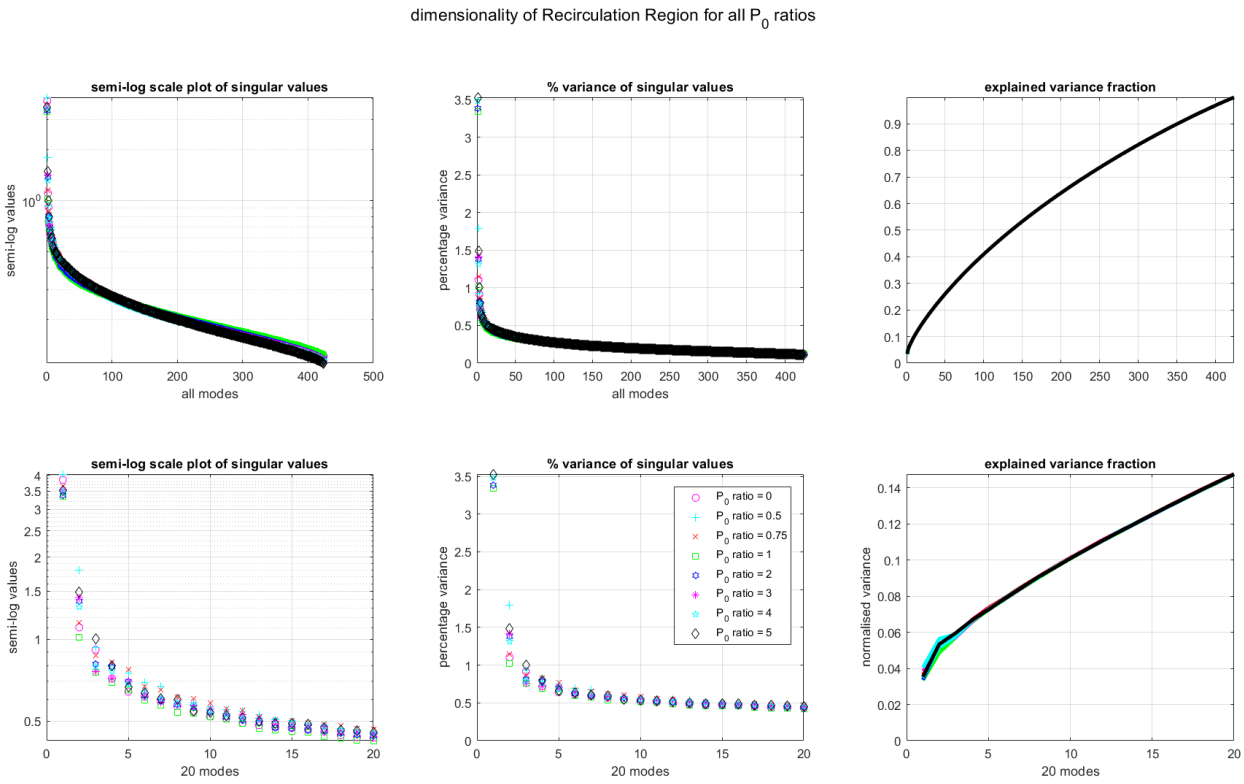


**Figure 30: Singular Values of Wake Region**

In this region, only the first three modes are analyzed because they have higher energies, compared to the subsequent modes, that are similar to the energy of the modes analyzed in previous sections.

PCA modes of the wake region are shown in Figure 31, which depicts the evolution of the first three modes with pressure ratio.

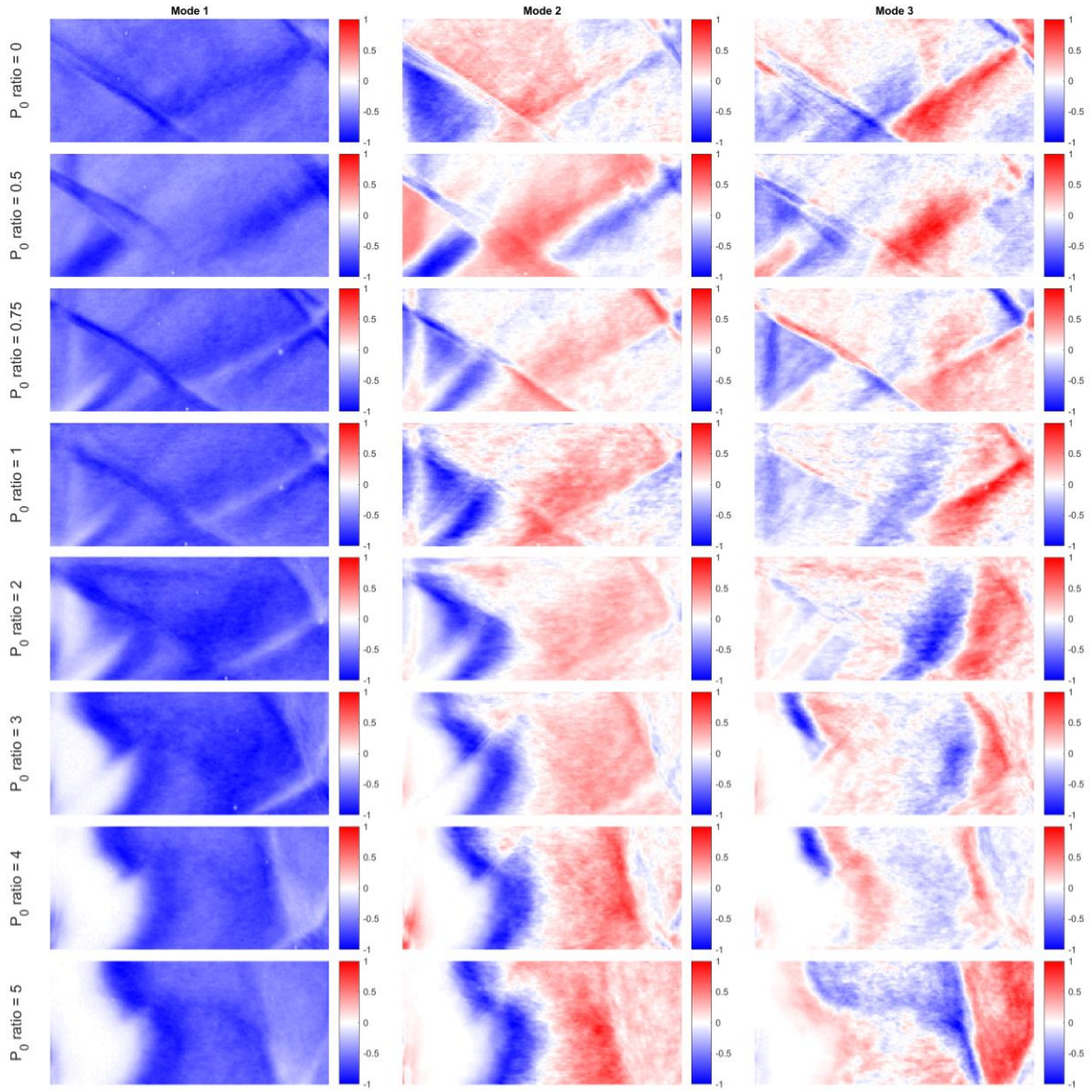


**Figure 31: Wake Region PCA Modes 1-3 across $P_{0_j}/P_{0_\infty}$ ratios**

It seems like the modes explore the wake region and oblique shock pattern behind the bow shock. Recall that there is an oblique initial shock coming off the retronozzle jet exit, which reflects off the pressure boundary of the freestream and then reflects off the physical boundary of the retronozzle jet. As $P_{0_j}/P_{0_\infty}$ ratio increases, the reflected shock angle increases and becomes more vertical. Also, the size of the wake increases as $P_{0_j}/P_{0_\infty}$ ratio increases, which can be interpreted from the increased area between the colored sections.

As $P_{0_j}/P_{0_\infty}$ ratios increase, the sections of the wake become messier and the oblique shock pattern becomes less obvious because the bow shock deflects the freestream flow more and oblique shocks may no longer be necessary to pressure match regions of the wake. This phenomenon is easily observed in Figure 15. Alternatively, this might be due to an inconsistency with data collection, or because the flow field is more complicated and interpretation is harder.

The fluctuations in image intensity where the sections alternate between blue and red, indicate a change in the horizontal density gradient which suggests some sort of opposite motion.

Mode 1 in Figure 31 is the mode related to mirror vibration, as previously mentioned.

Mode 2 in Figure 31 seems to focus on the upstream section of the region. It is interesting to note that the left and right sides of the images are the same color. This means that the density gradient of both reflected oblique shocks are of the same polarity, which suggests that the oblique shocks are moving in the same streamwise direction.

Mode 3 in Figure 31 seems to focus on the further downstream section of the region. Conversely, the left and right sides of the images are of opposing color, which suggests that the reflected oblique shocks move in opposite streamwise directions.

# 6. Conclusion

This thesis experimentally investigated the influence of stagnation pressure ratio between the jet and the freestream flow SRP flow steadiness. It was shown that the stagnation pressure ratio essentially characterizes the retronozzle jet expansion and affected the bow shock properties and steadiness in several ways. For the limiting case studied with no forebody and increasing stagnation pressure ratio, the bow shock standoff distance increased and the curvature decreased.

It was also observed that the bow shock was most unsteady for the case of the stagnation pressure ratio at unity with an almost perfectly expanded retronozzle jet. This was expected as it agreed with results from prior experiments. However, this bow shock unsteadiness was observed without obvious penetration of the bow shock, which demonstrates that the long-penetration mode is not required for unsteadiness. It also suggests that bow shock unsteadiness is a result of multiple mechanisms that should be explored further. For example, the presence of a forebody area could allow more unsteadiness to be observed.

Furthermore, the usefulness of Principal Component Analysis for the complicated SRP flow field was validated. With PCA modes, flow field structures of interaction and unsteadiness were identified, even though preliminary visual inspection only noted unsteadiness in the test case with unity stagnation pressure ratio. The energy of the modes were very low, which suggests that the structures would not have been easily detected with other methods. For instance, PCA identified bow shock motion harmonics and wake region wave interactions across all test cases.

Also, PCA on sub-regions proved helpful in examining regions in isolation that allowed more meaningful interpretation of mode, such as more focus on specific structures and motions.

# 7. Recommendations

This thesis recommends that individual investigation into other identified parameters be conducted, such as examining the influence of speed of sound ratio. Also, it seems that the presence of the forebody area adds an increased offset length to the bow shock standoff distance which would allow more unsteadiness to be observed and to test the effect of jet exhaust contact surface momentum.

Moreover, PCA modes suggested that they are various bow shock oscillation frequencies. A comparison between these frequencies with the frequencies of the motion of other structures could help provide insight on what might be influencing bow shock motion. This might also indicate the bow shock motion and unsteadiness is a coupled effect of other parameters.

Furthermore, the experimental set up can be improved with the a pulsed and more intense light source and Particle Image Velocimetry for quantitative flow visualization.

# 8. References


Barber, E. A. (1965). An Experimental Investigation of Stagnation-Point Injection. *Journal of Spacecraft and Rockets*.

Berry, S. A., Rhode, M. N., Edquist, K. T., & Player, C. J. (2011). Supersonic Retropropulsion Experimental Results from the NASA Langley Unitary Plan Wind Tunnel. *AIAA Thermophysics Conference.* Honolulu, Hawaii.

Charczenko, N., & Hennessey, K. W. (1961). *Technical Note D-751, Investigation Of Retrorocket Exhausting From The Nose Of A Blunt Body Into A Supersonic Free Stream* . National Aeronautics And Space Administration.

Daso, E. O., Pritchett, V. E., Wang, T.-S., Ota, D. K., & Blankson, I. M. (2007). The Dynamics of Shock Dispersion and Interactions in Supersonic Freestream with Counterflowing Jets. *AIAA Aerospace SCiences Meeting and Exhibit* . Reno, Nevada .

Finley, P. J. (1966). The flow of a jet from a body opposing a supersonic free stream . *Journal of Fluid Mechnaics* .

Hiyashi, K., Aso, S., & Tani, Y. (2005). Numerical Study of Thermal Protection System by Opposing Jet. *AIAA Aerospace Sciences Meeting and Exhibit.* Reno, Nevada.

Hu, H. (n.d.). *Semantics Scholar*. Retrieved from https://www.semanticscholar.org/: https://pdfs.semanticscholar.org/presentation/0af4/b234241b82c9f55ffeacb674d66595b874aa.pdf

Jarvinen, P. O., & Adams, R. H. (1970). *NAS 7-576, The Aerodynamic Characteristics Of Large Angled Cones With Retrorockets.* National Aeronautics And Space Administration .

Korzun, A. M., & Braun, R. D. (2010). Performance Characterization of Supersonic Retropropulsion for High-Mass Mars Entry Systems. *Journal of Spacecraft and Rockets*.

Korzun, A. M., Braun, R. D., & Cruz, J. R. (2009). Survey of Supersonic Retropropulsin Technology for Mars Entry, Descent and Landing. *Journal of Spacecraft and Rockets*.

Korzun, A. M., Cordell, C. E., & Braun, R. D. (2010). Comparison of Inviscid and Viscous Aerodyanmic Predictions of Supersonic Retropropulsion Flowfields. *AIAA/ASME Joint Thermophysics and Heat Transfer Conference.* Chicago, Illinois.

McGhee, R. J. (1971). *Technical Note D-6002, Effects Of A Retronozzle Located At The Apex Of A 140 Blunt Cone At Mach Numbers of 3.00, 4.50 And 6.00.* National Aeronautics And Space Administration.

Priebe, S., & Martin, M. P. (2012). Low-frequency unsteadiness in shock wave - turbulent boundary layer interaction. *Journal of Fluid Mechanics*.

Romeo, D. J., & Sterrett, J. R. (1963). Technical Note D-1605, Exploratory Investigation of the Effect of a Forward-Facing Jet on the Bow Shock of Blunt Body in a Mach 6 Free Stream. *National Aeronautics And Space Administration*.

Romeo, D. J., & Sterrett, J. R. (1965). Flow Field for Sonic Jet Exhausting Counter to a Hypersonic Mainstream. *AIAA Journal*.

Settles, G. S. (1949). *Schlieren And Shadowgraph Techniques.* Springer.

Shang, J., Hayes, J., Wurtzler, K., & Strang, W. (2001). Jet-Spike Bifurcation in High-Speed Flows. *AIAA Journal* .

Venkatachari, B. S., Cheng, G., Chang, C.-L., Zichettello, B., & Bilyeu, D. L. (2013). Long Penetration Mode Counterflowing Jets For Supersonic SLender Configuration - A Numerical Study . *AIAA Applied Aerodynamics Conference.* San Diego, CA.

Wang, C.-M. (1989). *Masters Thesis: Transient Flow Analysis of a Supersonic Ludwieg-Tube Wind Tunnel.* University of Texas, Arlington, Department of Aerospace Engineering.

Warren, C. H. (1959). An experimental investigation of the effect of ejecting a coolant gas at the nose of a bluff body. *Journal of Fluid Mechanics*.